Title

Amphibious surface-wave phase-velocity measurements of the Cascadia subduction zone

Journal

Geophysical Journal International, 217(3)

ISSN

0956-540X

Authors

Janiszewski, Helen A
Gaherty, James B
Abers, Geoffrey A
et al.

Publication Date

2019-06-01

DOI

10.1093/gji/ggz051

Peer reviewed

Geophysical Journal International

Geophys. J. Int. (2019) **217,** 1929–1948
Advance Access publication 2019 January 31
GJI Seismology

doi: 10.1093/gji/ggz051

Amphibious surface-wave phase-velocity measurements of the Cascadia subduction zone

Helen A. Janiszewski,[1,2] James B. Gaherty,[2] Geoffrey A. Abers,[3] Haiying Gao[4] and Zachary C. Eilon[5]

[1] *Department of Terrestrial Magnetism, Carnegie Institution for Science, Washington, DC* 20015*, USA. E-mail: hjaniszewski@carnegiescience.edu*
[2] *Lamont-Doherty Earth Observatory, Columbia University, Palisades, NY* 10964*, USA*
[3] *Department of Earth and Atmospheric Sciences, Cornell University, Ithaca, NY* 14853*, USA*
[4] *Department of Geosciences, University of Massachusetts - Amherst, Amherst, MA,* 01003*, USA*
[5] *Department of Earth Sciences, University of California - Santa Barbara, Santa Barbara, CA* 93106*, USA*

Accepted 2019 January 28. Received 2018 December 20; in original form 2018 July 20

SUMMARY

A new amphibious seismic data set from the Cascadia subduction zone is used to characterize the lithosphere structure from the Juan de Fuca ridge to the Cascades backarc. These seismic data are allowing the imaging of an entire tectonic plate from its creation at the ridge through the onset of the subduction to beyond the volcanic arc, along the entire strike of the Cascadia subduction zone. We develop a tilt and compliance correction procedure for ocean-bottom seismometers that employs automated quality control to calculate robust station noise properties. To elucidate crust and upper-mantle structure, we present shoreline-crossing Rayleigh-wave phase-velocity maps for the Cascadia subduction zone, calculated from earthquake data from 20 to 160 s period and from ambient-noise correlations from 9 to 20 s period. We interpret the phase-velocity maps in terms of the tectonics associated with the Juan de Fuca plate history and the Cascadia subduction system. We find that thermal oceanic plate cooling models cannot explain velocity anomalies observed beneath the Juan de Fuca plate. Instead, they may be explained by a $\leq$1 per cent partial melt region beneath the ridge and are spatially collocated with patches of hydration and increased faulting in the crust and upper mantle near the deformation front. In the forearc, slow velocities appear to be more prevalent in areas that experienced high slip in past Cascadia megathrust earthquakes and generally occur updip of the highest-density tremor regions and locations of intraplate earthquakes. Beneath the volcanic arc, the slowest phase velocities correlate with regions of highest magma production volume.

Key words: Mantle processes; North America; Seismic noise; Seismic tomography; Surface waves and free oscillations; Subduction zone processes.

1 INTRODUCTION

Subduction zones host a wide variety of processes that are central to the dynamic behaviour of the planet, including the evolution and modification of oceanic lithosphere prior to subduction; megathrust earthquakes and explosive volcanism; growth of continental crust through sedimentary and magmatic accretion and recycling of water, carbon and crustal materials into the deep mantle. Seismic images of the crust and mantle across and along subduction zones provide important constraints on these processes, both by characterizing the crustal and lithospheric architecture of the system and by quantifying critical parameters such as temperature, sediment distribution, and melt and volatile content. Regional-scale seismic analyses employing both active- and passive-source techniques have been highly successful in resolving localized portions of the subduction system, including on the incoming plate (e.g. van Avendonk *et al.* 2011; Tian *et al.* 2013; Bell *et al.* 2016; Han *et al.* 2016; Horning *et al.* 2016; Canales *et al.* 2017), across the megathrust (e.g. Trehu *et al.* 1994; Parsons *et al.* 1998; Nedimovic *et al.* 2003; Li *et al.* 2015), and along and across the forearc, arc and backarc regions (e.g. Shillington *et al.* 2004; Wiens *et al.* 2008; Abers *et al.* 2009; Audet *et al.* 2009; Wagner *et al.* 2010; Calkins *et al.* 2011; Porritt *et al.* 2011; Wei *et al.* 2016). Prior to the recent deployment of amphibious arrays, seismic images of entire subduction systems have generally been limited to global models (e.g. Kustowski *et al.* 2008; Ritsema *et al.* 2011; French *et al.* 2013; Moulik & Ekström 2014), which lack the resolution to distinguish across and along-strike variations within these highly heterogeneous systems.

The Cascadia Initiative (CI) experiment (Toomey *et al.* 2014) enables the study of the Cascadia subduction zone using seismic instrumentation extending from the Juan de Fuca ridge offshore to

beyond the Cascades volcanic arc, from northern California to the Canadian border (Fig. 1). The experiment spans the young (0–10 Ma) oceanic Juan de Fuca and Gorda plates from the ridge to the trench, a sediment-rich accretionary continental shelf, a forearc consisting of accreted terranes including the uplifted Olympic Peninsula and the coast ranges of Washington and Oregon, the Cascades volcanic arc and a broad backarc region that transitions from stable continental crust in the north to active extension in the Basin and Range province to the south. Emerging results from CI and related analyses suggest that the Juan de Fuca plate is formed at a hot, asymmetric, spreading centre with ∼ 1–2 per cent partial melt that either quickly cools or solidifies through downwelling beneath the centre of the plate (Tian *et al.* 2013; Bell *et al.* 2016; Gao 2016; Byrnes *et al.* 2017; Eilon & Abers 2017). Intraplate structural heterogeneity associated with palaeoridge migration (Wilson 1993) is interpreted as enhanced localized cooling and/or hydration (Bell *et al.* 2016; Han *et al.* 2016; Horning *et al.* 2016; Canales *et al.* 2017). Surface-wave and receiver-function imaging suggests variable amounts of sediment and/or fluids at the megathrust interface (Janiszewski & Abers 2015; Gao 2016). Body-wave tomographic imaging of the upper mantle beneath the forearc indicates low-velocity regions that have been interpreted as accumulated melt-rich material in the asthenosphere beneath the subducting slab (Hawley *et al.* 2016; Bodmer *et al.* 2018).

In this study, we present a comprehensive set of Rayleigh-wave phase-velocity maps from 9 to 160 s period spanning the Cascadia subduction region. We focus on phase-velocity maps, rather than an inversion for 3-D shear-velocity structure, for two reasons. First, regional phase velocities represent a basic observation that can be derived directly from seismic waveforms with minimal assumptions or choices by the analyst. Therefore, they can be relatively easily compared to other phase-velocity observations from different regions (e.g. James *et al.* 2014; Godfrey *et al.* 2017) or to alternative models from the same region (e.g. Foster *et al.* 2014; Jin & Gaherty 2015). In contrast, regional shear-velocity models require a variety of critical decisions on the inversion process, such that subsequent comparison between models results in an ambiguity of whether differences are required by the data or result from modelling choices. Second, they can be easily modelled for a variety of material parameters (e.g. Ma & Dalton 2017), including temperature, composition, crustal architecture and sediment distribution. Our phase-velocity models show marked coherent heterogeneity both on- and off-shore. We analyse the variations on the Juan de Fuca plate, the subduction-zone forearc region and along the Cascades arc, and we discuss possible relationships between variations in the three regions in the context of the underlying thermal, compositional and deformation processes.

2 METHODS

2.1 Instruments and data

We construct fundamental-mode Rayleigh-wave phase-velocity maps that image the Cascadia subduction zone. They are derived at short periods (9–20 s) from ambient-noise correlation, providing constraints on the crust and shallow upper mantle, and at longer periods (20–160 s) from earthquake data, providing constraints spanning the lithosphere and upper asthenosphere. These data sets are recorded on broad-band ocean-bottom seismometers (OBSs) and onshore instruments from all four years of the CI (Toomey *et al.* 2014), as well as a subset of sites from the Blanco and Gorda OBS experiments (Nabelek & Braunmiller 2013) and other networks (Fig. 1). Combined, these comprise an array with ∼70 km station spacing (or less in focus regions) extending from the Juan de Fuca ridge to the east of the Cascades volcanic arc. Each of the OBS instruments is also equipped with a pressure sensor, either a differential pressure gauge or an absolute pressure gauge.

2.2 Earthquake Rayleigh-wave processing

We calculate phase-velocity maps from regional and teleseismic surface-wave observations following the method of Jin & Gaherty (2015), which uses frequency-dependent phase-delay and amplitude measurements to calculate phase-velocity maps via the Helmholtz equation (Lin & Ritzwoller 2011). The initial data set consists of all earthquakes with $M_w \geq 6.5$ and epicentral depth < 50 km that occurred between 5° and 125° from each station, yielding a total of 208 earthquakes. The data are bandpass filtered between 10 and 200 s period, downsampled to one sample per second and converted to displacement by deconvolving the instrument response.

For each earthquake, the vertical-component Rayleigh waves are windowed in time (Fig. 2) following the method outlined in Jin & Gaherty (2015) prior to calculating the cross-correlations between station pairs. Broad-band cross-correlation functions (CCFs) are calculated for all station pairs with interstation distances < 200 km. This interstation distance range is chosen to minimize errors due to cycle skipping. The CCFs are narrow-band filtered using a 10 per cent width Gaussian filter centred on the periods of interest: 20, 25, 32, 40, 50, 60, 80, 100, 115, 130, 145 and 160 s. Phase delays for each station pair are measured from the narrow-band CCFs using a Gaussian wavelet, and wavefield amplitude at each station is estimated from the autocorrelation at each narrow-band frequency (Jin & Gaherty 2015). The collection of multichannel phase delays is checked for internal consistency and cycle skipping, which is eliminated by comparing the apparent interstation delays with plausible model dispersion. After these quality-control steps, 183 earthquakes are retained (Fig. 3).

The phase delay times at each period are used to calculate apparent phase-velocity maps for each earthquake using the Eikonal equation (Lin *et al.* 2009). Since the Eikonal equation relates traveltime gradient to apparent phase velocity, the estimated apparent phase velocity can be biased by focusing and defocusing. The Helmholtz equation uses amplitude information to correct apparent phase-velocity measurements for these effects, producing estimates of true structural phase velocities (Lin & Ritzwoller 2011). A comparison of the Eikonal and Helmholtz phase-velocity maps is presented in the Supporting Information. We use the observed Rayleigh-wave amplitudes at each station to estimate the Helmholtz correction at each frequency using a surface-fitting technique (Jin & Gaherty 2015). Short-wavelength amplitude variability associated with inaccurate instrument response or anomalous site effects are removed using station terms determined by averaging over all events (Accardo *et al.* 2017). The Helmholtz-corrected phase-velocity maps are calculated for each earthquake and then stacked to determine final structural phase-velocity maps for the entire array.

2.2.1 Compliance and tilt corrections

Signals measured on the seafloor benefit from the reduction of compliance and tilt noise prior to processing. Compliance noise is produced by the deformation of the seafloor in response to the loading from long-wavelength infragravity ocean waves at the water surface

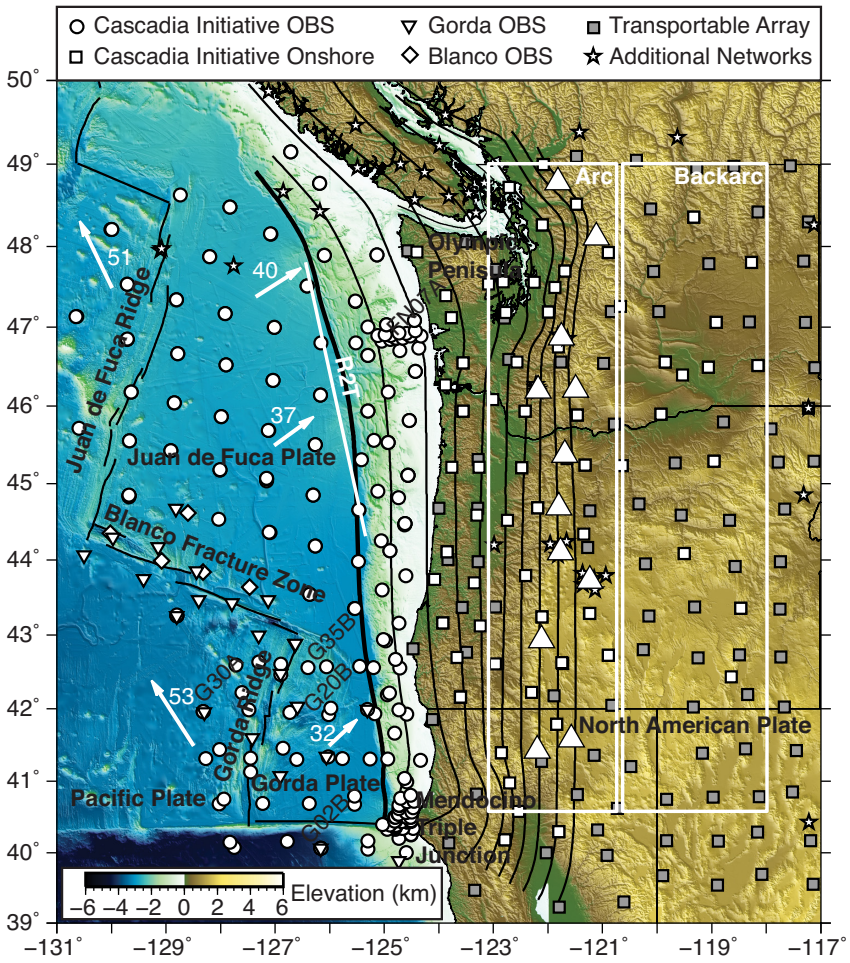

Figure 1. Map of the Cascadia subduction zone showing locations of seismic stations. Large triangles indicate the Cascades volcanoes and arrows indicate plate motions relative to North America in mm yr^{-1} (DeMets *et al.* 2010). The deformation front is represented by a thick black line; thinner black lines are 10 km depth contours to the top of the subducting Juan de Fuca crust (McCrory *et al.* 2012). The deformation-front-parallel transect from the active-source ridge-to-trench experiment is shown as the white line labelled R2T, which gives local constraints on sediment properties (Han *et al.* 2018). The white boxes labelled arc and backarc are the regions where average phase velocities are calculated for Fig. 18.

and can be reduced in the vertical seismogram by using a collocated pressure sensor (Crawford & Webb 2000). The magnitude of compliance noise is frequency dependent, with an observable signal that extends from a low frequency below the capability of the broad-band seismometers (i.e. below 0.005 Hz) to a high-frequency limit that is controlled by the water depth. The maximum frequency for the infragravity wave signal can be estimated by

$$f_{\max} \approx \sqrt{\frac{g}{2\pi d}}$$

where g is the gravitational acceleration and d is the OBS deployment depth (Bell *et al.* 2014). The OBSs used here are deployed in water depths that range from 52 to 4464 m, which implies that the highest frequencies affected by compliance noise will range from $\sim$ 0.019 to 0.173 Hz or periods of 6 to 52 s. This overlaps with the 20–160-s-period band of interest. Tilt noise is due to bottom currents acting on the instruments and can be corrected via a transfer function between the vertical and the two horizontal components sequentially (e.g. Crawford & Webb 2000), or between the vertical and the calculated maximum horizontal direction of the tilt noise (e.g. Bell *et al.* 2014).

To accurately determine compliance and tilt corrections, sections of data that contain transient signals (e.g. local or teleseismic earthquakes, instrument glitches) are removed prior to calculating the transfer functions. We develop and employ a two-step automated quality-control method that removes sections of data contaminated by transient signals (Fig. 4), allowing accurate daily transfer function calculations. Once high-quality spectra are determined for each station, the appropriate transfer functions are calculated for tilt and compliance noise removal (Fig. 5). Details on the corrections and any additional pre-processing steps applied to each station are provided in the Supporting Information.

2.3 Ambient-noise processing

To calculate phase-velocity maps from ambient-noise cross-correlograms, we adapt the frequency-domain method using Aki's formulation (Aki 1957) described in Ekström *et al.* (2009) and Jin *et al.* (2015). We utilize the daily, vertical-component broad-band cross-correlograms between all station pairs produced by Gao & Shen (2015). Daily cross-correlations are stacked for each station pair; OBS stations that reoccupy the same site within 500 m over

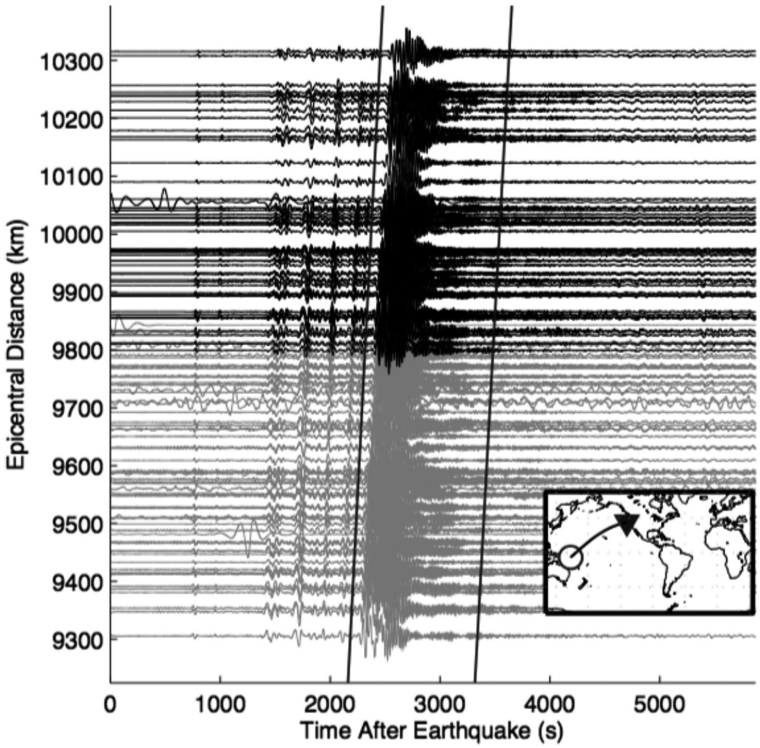

Figure 2. Surface-wave data recorded for the M_w 7.5 Solomon Islands earthquake on 2014 April 19. The traces are bandpass filtered between 10 and 200 s, and tilt and compliance corrections have been applied. Black traces indicate onshore seismometers; grey traces indicate OBSs. The black vertical lines indicate the window function isolating the Rayleigh-wave signal. The inset map indicates the earthquake origin (circle) and the array (upside down triangle) locations.

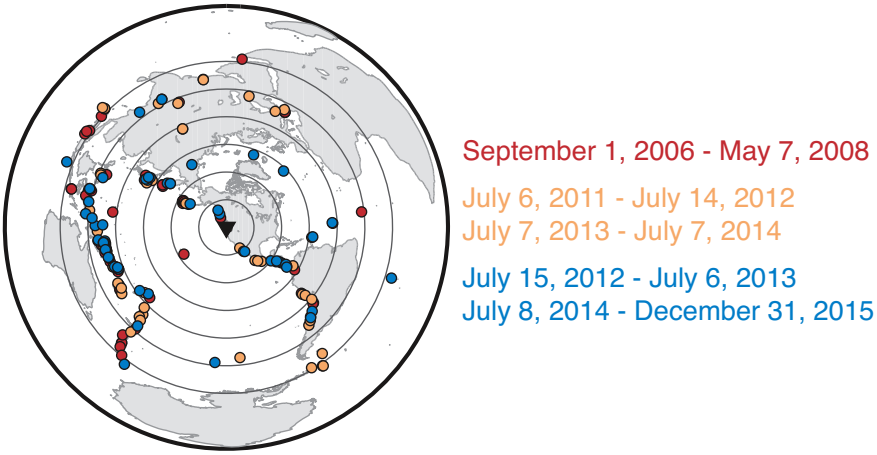

Figure 3. Earthquake distributions centred around the array for three time periods corresponding to the deployment durations of the TA network (2006–2008), when the Cascadia Initiative array was in its northern configuration (2011–2012, 2013–2014) and in its southern configuration (2012–2013, 2014–2015).

multiple deployment years are stacked together (Supporting Information).

There is evidence of clear Rayleigh-wave signals in the stacked cross-correlations in the expected velocity window (defined between 1.8 and 5.5 km s^{-1}), including the OBS data (Fig. 6). The only exceptions to these clear signals are observed at several of the shallow water OBSs deployed on the continental shelf. Here, a decrease in ambient-noise cross-correlation quality is likely due to compliance noise affecting the microseism band at shallow water depths (Webb & Crawford 2010; Tian & Ritzwoller 2015). We do not observe any widespread evidence of fundamental-mode Rayleigh waves travelling within the water column (also referred to as Scholte waves); such coupled modes are typically observed at periods < 10 s (e.g. Harmon *et al.* 2007; Yao *et al.* 2011; Bowden *et al.* 2016), which is shorter than our main observations.

A phase-velocity curve is determined for each station pair by relating the real part of the spectrum of the cross-correlogram to a modulated Bessel function scaled to the frequency-dependent phase velocity, using a waveform-fitting algorithm (Jin *et al.* 2015; e.g. Fig. 7). This method improves upon the zero-crossing method of Ekström *et al.* (2009) for close station distances where few zero crossings exist. The waveform fitting is sensitive to the initial dispersion curve assumed for the fitting, and we found that the inversion can be stabilized by first using initial dispersion curves for each station pair derived from the zero-crossing method, rather than generic regional *a priori* dispersion curves. This approach increases

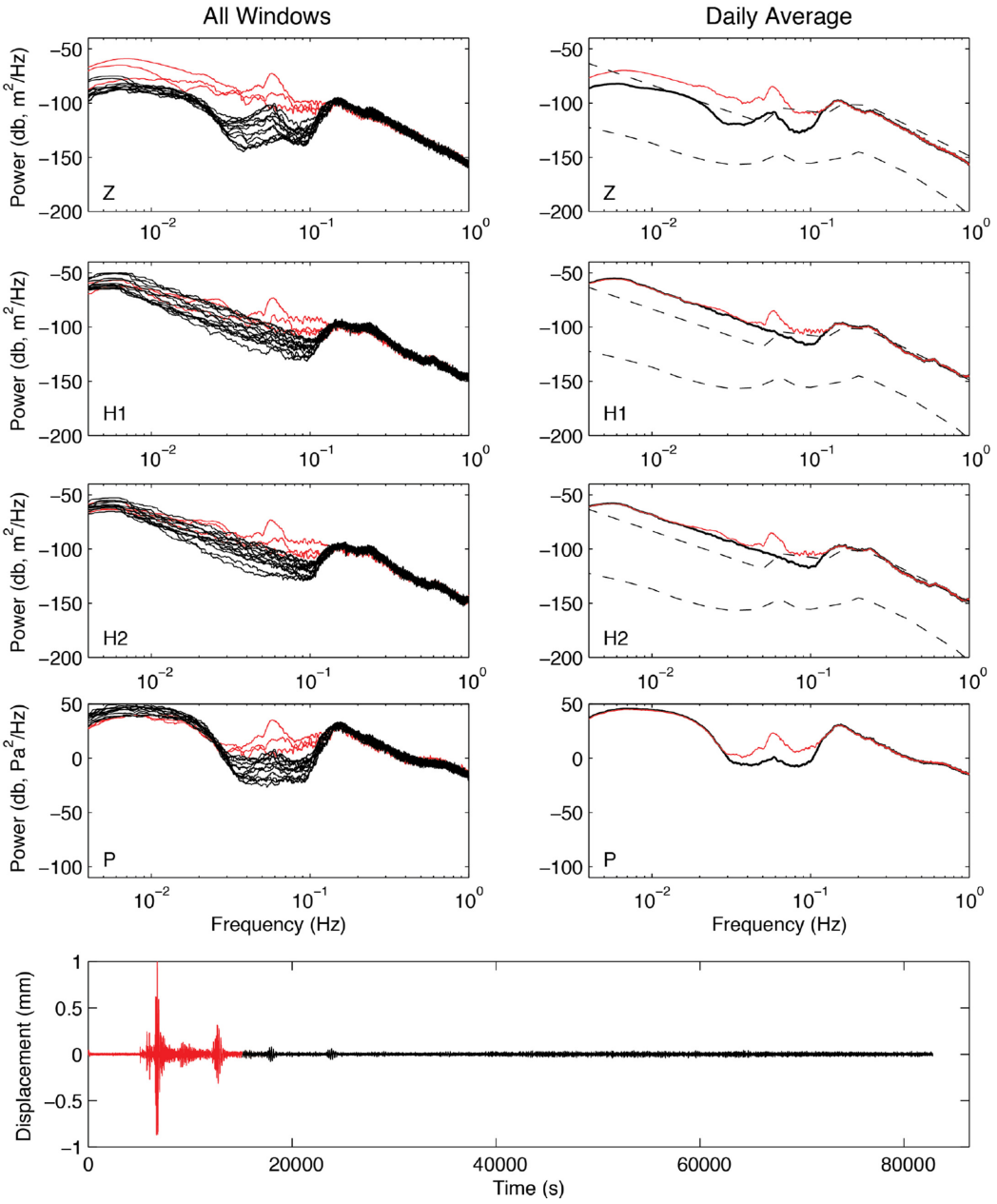

Figure 4. Power spectral density (PSD) functions from station G02B (location shown in Fig. 1) for the Z (vertical), H1, H2 (horizonal) and P (pressure) components for 2013 February 6, which includes several M_w 7.0+ earthquakes originating in the Santa Cruz Islands. The corresponding time-series is plotted at the bottom. The left column shows PSDs calculated from each 7200-s-long window. Red lines indicate PSDs that are flagged as bad due to the presence of transient signals, corresponding to the red regions in the time-series, while black PSDs are flagged as good. The right column plots the daily-average PSDs. The red PSD includes all windows, while the black only includes windows flagged as good. Dashed lines represent the high and low noise models (Peterson 1993).

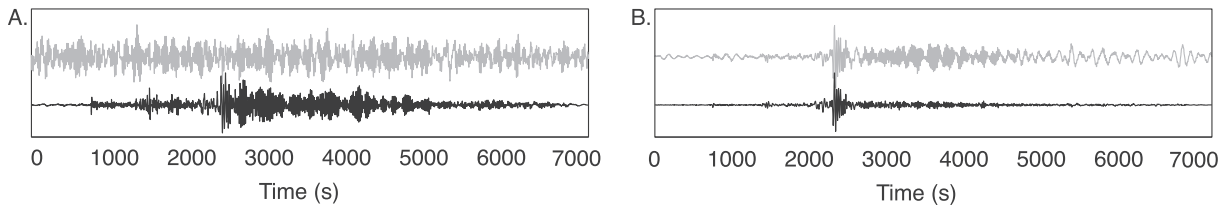

Figure 5. Seismograms of the Vanuatu 2012 February 2 M_w 7.0 earthquake. The data are bandpass filtered from 10 to 200 s; the original seismogram is shown in grey and the tilt and compliance corrected seismogram is shown in black. (a) Seismograms from FN07A, trawl-resistant mount design instrument deployed in 154 m of water. (b) Seismograms from G30A, which is deployed in 3124 m of water. Station locations as shown in Fig. 1.

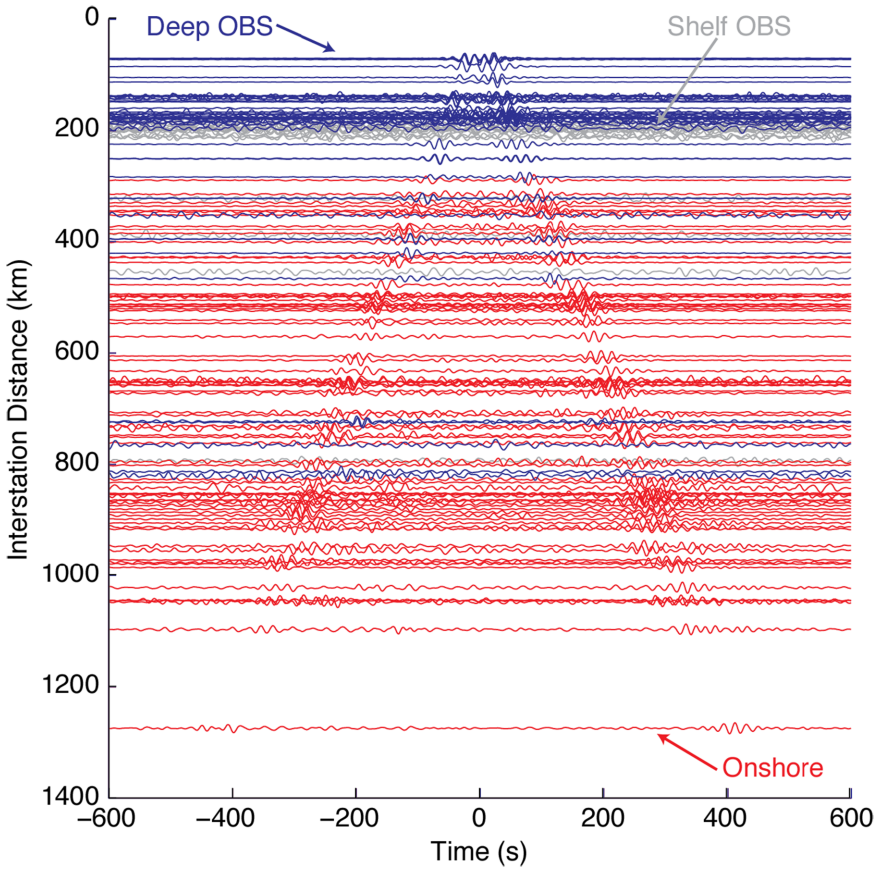

Figure 6. Cross-correlation functions of ambient-noise data with the OBS G20B (location shown in Fig. 1) filtered from 8 to 25 s. Traces are coloured blue for a deep OBS pair (≥500 m water depth), grey for a shelf OBS pair (<500 m water depth) and red for an onshore station pair.

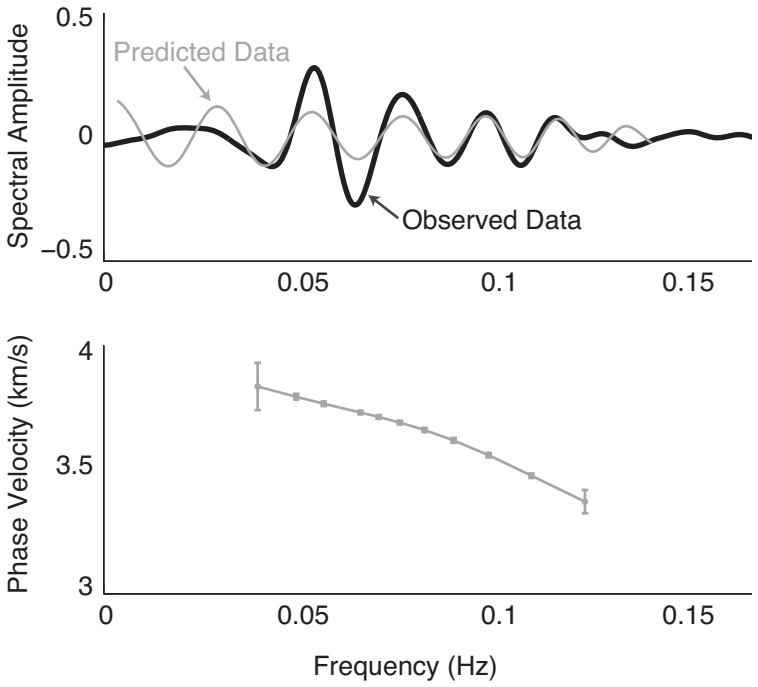

Figure 7. Example of fitting the modulated Bessel function to calculate the phase-velocity curve for the OBS–OBS station pair, G20B-G35B. Station locations as shown in Fig. 1.

the number of successful dispersion measurements while simultaneously decreasing the average misfit of the Bessel functions by ∼16 per cent.

We invert the station-pair phase-velocity observations for phase-velocity maps at periods of 9, 10, 11, 12, 13, 14, 15, 17.5 and 20 s, using finite-frequency sensitivity kernels (e.g. Lin & Ritzwoller 2010) approximated to include only the inner two Fresnel zones. Interstation phase-velocity measurements, expressed as slowness perturbations from a reference average velocity, are weighted by errors estimated from the dispersion-curve inversion. The prior error is calculated as a standard estimate of data uncertainty from the residuals (Crosbie 2018). We use a constant phase velocity calculated from the weighted average from all station pairs at a given period as the starting model; however, we test a range of constant initial velocities ($\pm$ 0.5 km s^{-1}) and observe no significant effects on the final result. A first-derivative smoothing constraint is applied; the smoothing factor is determined through a series of L-curve tests at each period. Only station pairs with cross-correlations that have a signal-to-noise ratio $\geq$ 5 after stacking the forward- and reverse-time directions for the expected Rayleigh-wave window, and with interstation distances $\geq$ 20 km are used at all periods. To avoid errors associated with the noise of the shelf OBS instruments, OBSs at depths shallower than the predicted depth for compliance noise at 20 s period (624 m) are excluded from the inversion.

3 RESULTS

The phase-velocity maps (Fig. 8) reflect the major tectonic features of the Cascadia region: the Juan de Fuca and Gorda ridges, the contrast between faster velocity oceanic lithosphere and slower continental forearc lithosphere, slow velocities beneath the volcanic arc and the faster subducting plate. Features are well resolved in both the onshore and offshore regions. Additional maps of phase velocities, uncertainties, ray-path densities and resolution tests are provided in the Supporting Information.

3.1 Quality of the offshore measurements

With the exception of the 9 s period constrained by ambient-noise data, average uncertainties in the phase-velocity maps are higher in the offshore areas than onshore (Fig. 9). For periods constrained by the earthquake data, uncertainties are estimated as a standard error of the mean of the event-based phase velocity within each pixel. For periods constrained by ambient-noise data, the result is bootstrapped by resampling with replacement the original station-pair phase velocity measurements, using identical parameters over 1000 iterations; uncertainties are estimated as a standard deviation of these results (e.g. Calkins *et al.* 2011). While the uncertainties for the two data sets are not directly comparable due to the differing measures of error appropriate for the given analysis, variations in uncertainty are meaningful within the data sets. With the exception of the very long-period offshore data ($T > 100$ s), the uncertainties are less than 15 per cent of the total range of the data. In general, these results suggest that we are able to robustly image both environments at a wide range of periods.

3.2 Comparison of earthquake and ambient-noise results

The Rayleigh-wave signal-to-noise level falls off rapidly at periods longer than 20 s for the ambient-noise CCFs, and at periods shorter than 20 s for the earthquake seismograms. As a result, the phase velocity maps from the two techniques overlap only at 20 s. Ideally, minimal variation should exist between the phase velocity maps at 20 s calculated using the two data sets since they are sensitive to the same structures. The mean absolute difference between the two 20 s phase velocity maps is 0.1017 km s^{-1} (Fig. 10). This is larger than the average uncertainty of the measurements, but is still small relative to the 0.95 km s^{-1} total range of the 20 s phase velocity map (Fig. 8). However, differences of > 0.4 km s^{-1} are observed in some locations, particularly near the coastline and southeast corner of the map; the discrepancy is larger than observed in other studies that have combined these techniques (Lin & Ritzwoller 2011; Jin & Gaherty 2015; Jin *et al.* 2015; Accardo *et al.* 2017) and reflects ambient-noise phase velocities that are slower than the earthquake-based results. The region near the coastline is less well constrained using the ambient-noise data since shallow OBS sites are not used. Similarly, since the ambient-noise data set does not incorporate the transportable array data deployed from 2006–2008, the southeast corner of the region is also sparsely covered (Fig. 1). The effect of this difference in station distribution is reflected in the resolution maps (see the Supporting Information), which show relatively decreased resolution in these regions for the 20-s-period ambient-noise phase-velocity maps; this decrease is not shown for the 20 s earthquake-based resolution maps. Thus, the largest differences are likely in part due to differences in data coverage, which was absent from previous studies using similar methodologies (e.g. Jin *et al.* 2015; Accardo *et al.* 2017; Crosbie 2018). Furthermore, the 20-s-period phase-velocity maps for both the ambient-noise and Helmholtz results have higher average uncertainties relative to their adjacent periods. This implies that the data quality is relatively poor at the 20 s period for both data sets; the difference between the phase velocity maps may reflect this.

3.3 Comparison with previous studies

We compare our amphibious phase velocity maps with previous results for Cascadia that have used either entirely onshore or offshore data, encompassing both ambient-noise and earthquake-based surface waves (Fig. 11; Wagner *et al.* 2010; Porritt *et al.* 2011; Jin & Gaherty 2015; Bell *et al.* 2016). We observe good agreement with our results, particularly in relation to major tectonic features. One region with significant differences is the forearc, which is expected because previous studies are not amphibious. Compared to the onshore results (Figs 11b–d), we more clearly resolve two distinct strike-parallel lines of slow velocities—one beneath the volcanic arc and the other along the coastline, separated by a region of higher velocities. These slowest velocities ($<$3.6 km s^{-1}) along the coastline are not imaged by the offshore result, although they extend offshore in our maps (Figs 11a and e). This demonstrates the improvement in resolution of the forearc and even the transition into the volcanic arc by using an amphibious data set. Furthermore, these forearc patterns are similar to those observed in onshore-offshore models of shear velocity (e.g. Gao 2016; Rathnayaka & Gao 2017; Gao 2018), although the phase velocities are not directly comparable to depth slices. Another significant difference is between the velocities of the Gorda plate observed by the offshore result (Figs 11a and e); Bell *et al.* (2016) image slower velocities beneath the entire Gorda plate. Bell *et al.* (2016) utilize an age-dependent starting model, and our result incorporates an additional year of OBS stations on the southern half of the study area, both of which may contribute to this difference.

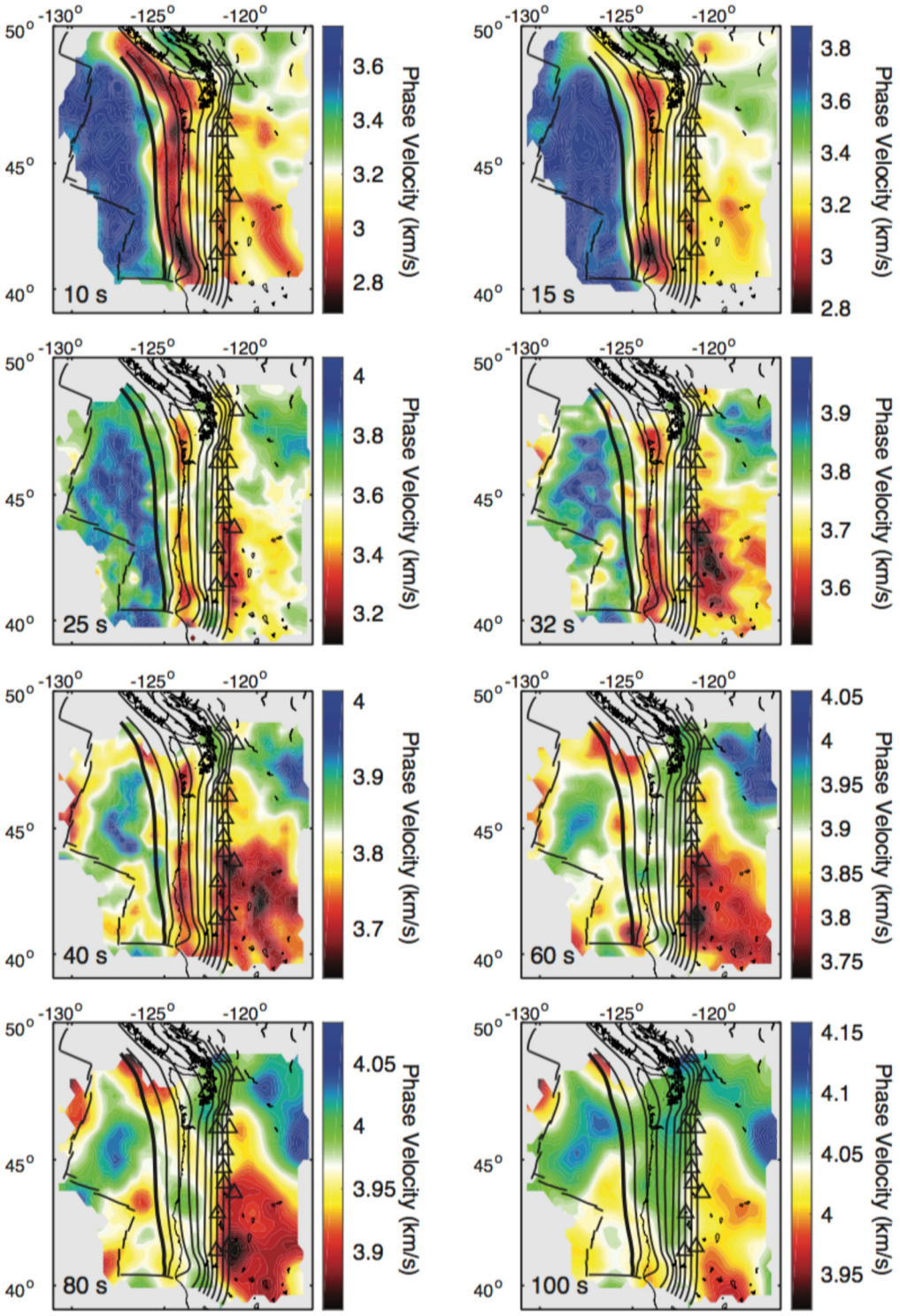

Figure 8. Phase-velocity maps from both ambient-noise (10 and 15 s) and earthquake (20–100 s) data. Black lines and triangles are the same as Fig. 1.

4 DISCUSSION

Shear-velocity sensitivity kernels are calculated using the program *surf96* (Herrmann & Ammon 2004; Herrmann 2013) for three different velocity models to guide interpretations of the phase velocity maps and better understand the effects of structural variation across the array (Fig. 12). We generate a continental model based on the starting model from Calkins *et al.* (2011), who inverted ambient-noise CCFs in a part of this region. Over oceanic crust we use a model with 3 km of water and 0.1 km of sediment overlying 6 km of crust, where sediment shear velocity is constrained by the empirically observed relationship between sediment thickness and V_s in Cascadia (Ruan *et al.* 2014; Bell *et al.* 2015; Bell *et al.* 2016), and crustal and upper-mantle velocities are consistent

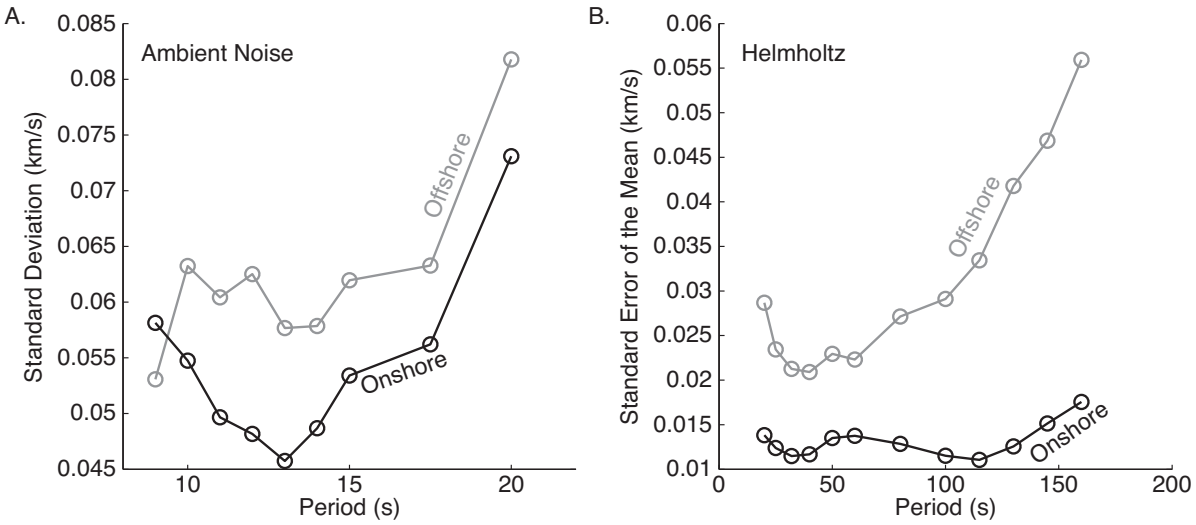

Figure 9. Comparison of average uncertainties at each period for onshore and offshore regions of the phase-velocity maps for the (a) ambient-noise and (b) Helmholtz results. Averages are calculated as the mean of all grid points for the two regions in the resultant maps (Supporting Information).

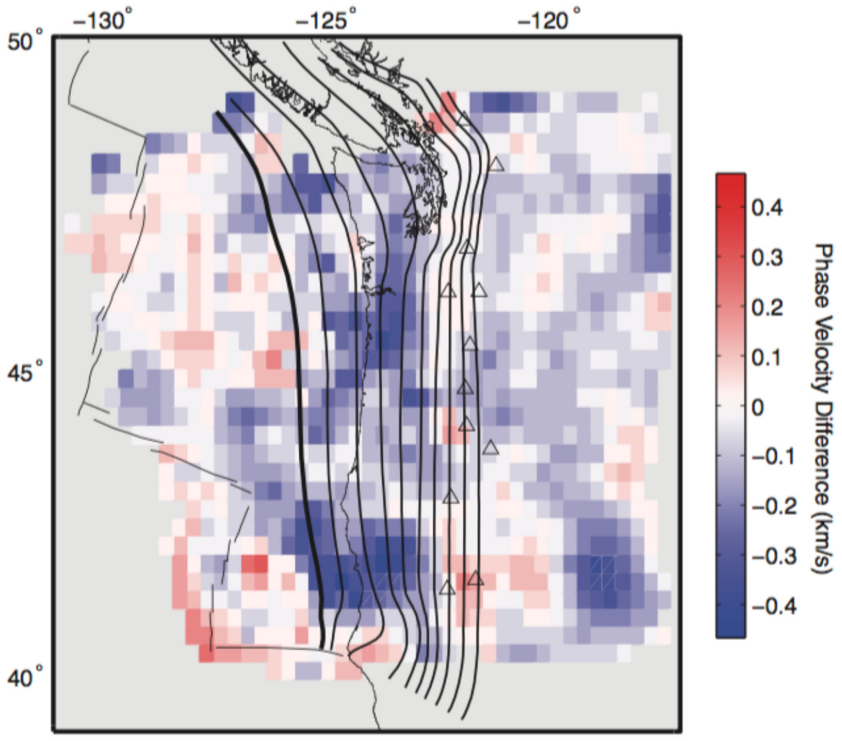

Figure 10. Difference in phase-velocity between the 20 s results from the ambient-noise and earthquake data. Negative values (blue colours) indicate that the ambient-noise data produced a slower result. Black lines and triangles are the same as Fig. 1.

with young oceanic lithosphere (Gaherty & Dunn 2007). For the accretionary wedge, we construct a model with 100 m of water, and a 7.5 km thick accretionary wedge overlying the oceanic crust and mantle; wedge velocities are consistent with those observed landwards of the deformation front in active-source studies (e.g. Horning *et al.* 2016) converted to shear velocities using empirical relationships (Castagna *et al.* 1985; Brocher 2005) and satisfy *P*- and *S*-wave delay times used in sediment-property calculations (e.g. Rychert *et al.* 2018). This representative model for the accretionary wedge has the subducting Moho located at 13.7 km below sea level, which is within the observed range of Moho depths beneath the Cascadia margin offshore (Janiszewski & Abers 2015; Horning *et al.* 2016).

Sensitivity kernels at all periods are similar for the oceanic and continental models indicating that phase velocities in these regions at a given period can be inferred to be sensitive to similar depth ranges to first order. However, for the continental shelf, the low velocities in the shallowest 10 km significantly affect the sensitivity

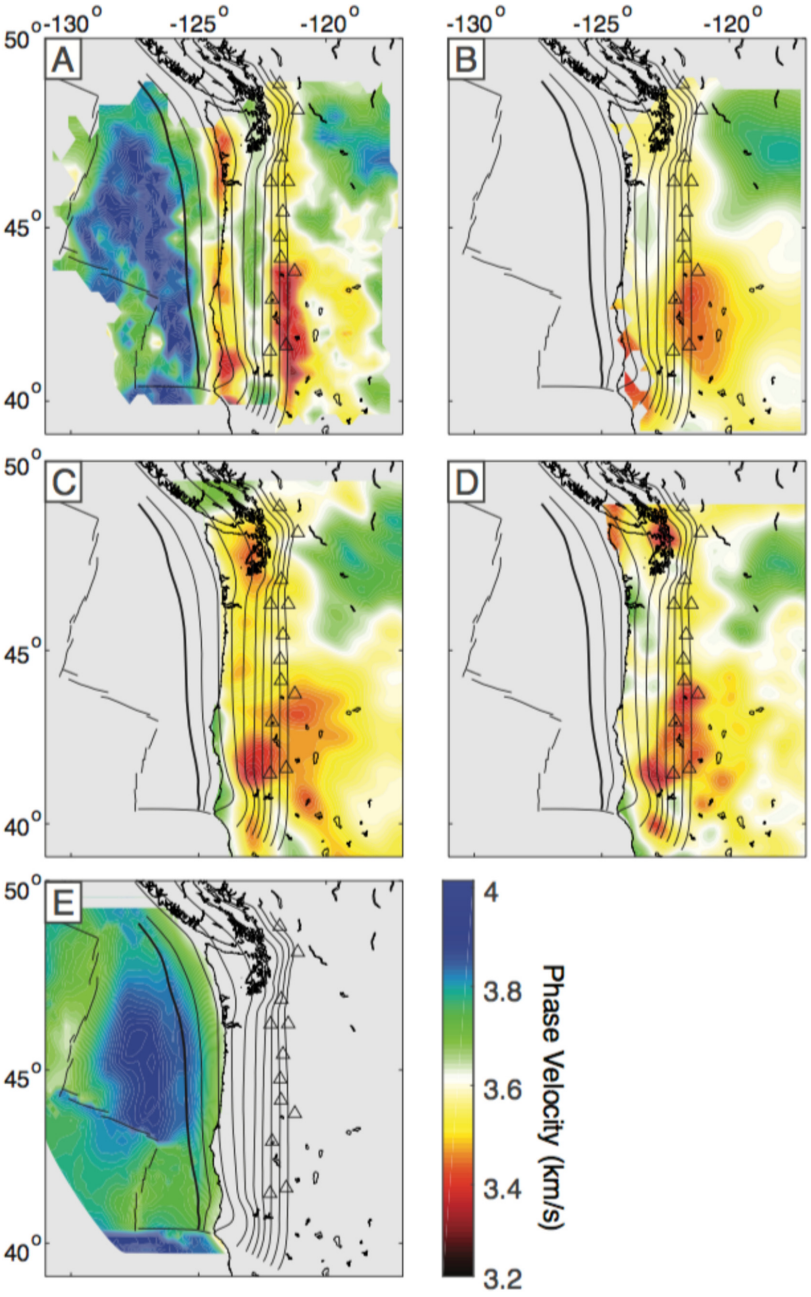

Figure 11. Comparison of 25-s-period phase-velocity maps from this and previous studies. (a) This study. (b) Jin & Gaherty (2015) using the Helmholtz equation for earthquake data onshore. (c) Porritt *et al.* (2011) using ambient-noise data onshore. (d) Wagner *et al.* (2010) using the two-plane wave method (Forsyth & Li 2005) for earthquake data onshore. (e) Bell *et al.* (2016) using the two-plane wave method for earthquake data offshore. Black lines and triangles are the same as Fig. 1.

kernels for periods from 10 to 20 s, shifting peak sensitivities for periods of 20 s or less into the upper 10 km. This model does not represent the entire accretionary wedge; the kernels should be more similar to the oceanic crust kernels close to the trench, and lithification of the wedge as it thickens may produce faster velocities at depth closer to the coast. However, the comparison does show strong changes in depth sensitivity at these periods associated with crustal structure, and highlights the need for careful evaluation of phase velocity maps independent of any complex, highly nonlinear inversion for shear velocity. Periods longer than 32 s have similar sensitivity kernels for each of the three different models.

4.1 Structure of the oceanic plate prior to subduction

From 10 to 25 s period the fastest phase velocities are seaward of the deformation front, within the oceanic plate (Fig. 8). At these periods oceanic phase velocities are sensitive to the mantle, whereas within the continent these periods sample the crust (Fig. 12), explaining the significantly slower velocities landward of the deformation front. This dichotomy diminishes at longer periods where phase velocities in both geographic regions sample mantle. Slow phase velocities are located along the axis of the Juan de Fuca and Gorda ridges relative to the plate interior at all periods, although most clearly observed from 25 to 80 s. There is some asymmetry with slower velocities

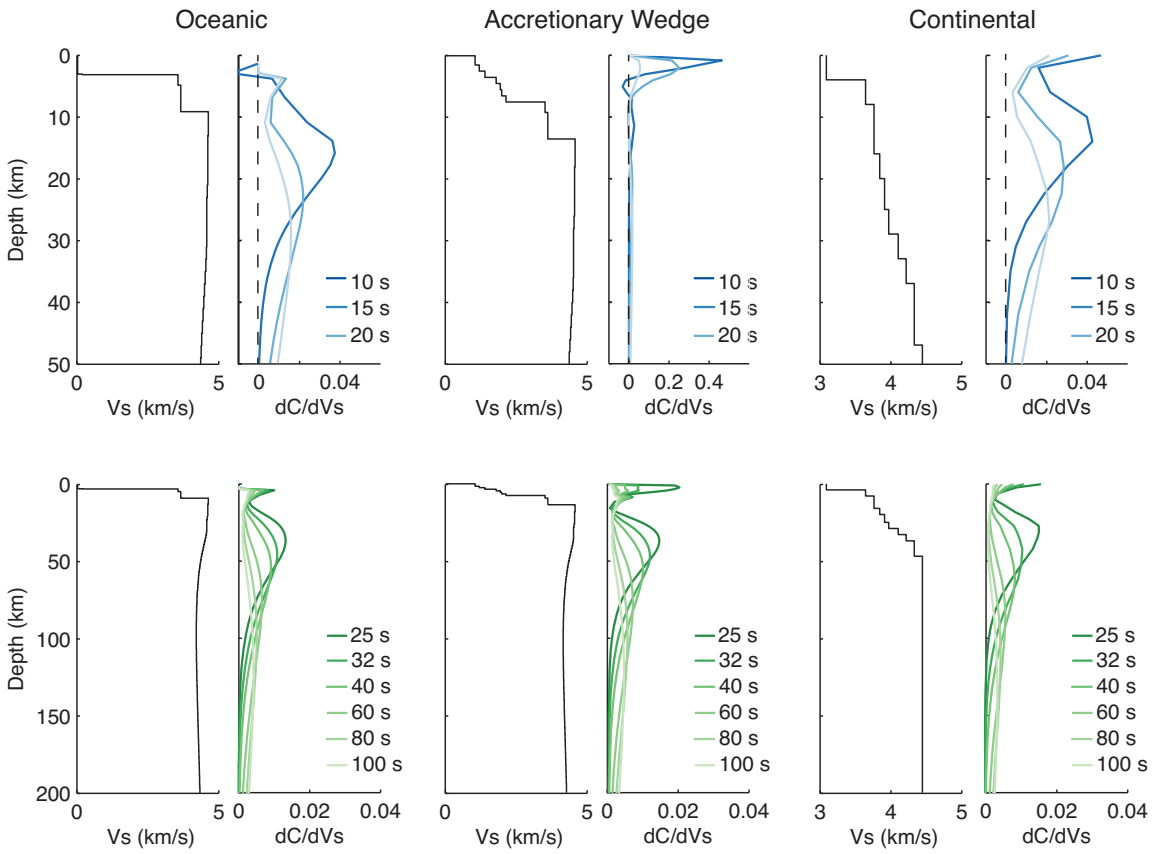

Figure 12. Predicted sensitivity kernels as dC/dV_s, the derivative of fundamental-mode Rayleigh-wave phase velocity (C) with respect to shear velocity (V_s), for three starting shear velocity models: oceanic (with 3 km water depth), accretionary wedge (with 0.1 km water depth) and continental. The top row shows kernels for 10, 15 and 20 s period, and is zoomed into the upper 50 km; the bottom row extends to 200 km and shows kernels from 25 to 100 s. Note that the scale of the 10–20 s kernels has changed for the accretionary wedge.

west of the Juan de Fuca ridge, consistent with previous surface wave observations (Bell *et al.* 2016). However, this feature is on the edge of the phase-velocity maps and not well resolved, so we do not interpret it further.

Within oceanic plates the phase velocity is expected to vary with plate age. Previous measurements have typically focused on larger oceanic basins including the Pacific (Nishimura & Forsyth 1988), the Atlantic (James *et al.* 2014), and the Indian (Godfrey *et al.* 2017). Our data set offers the opportunity to compare these measurements with a significantly smaller and younger plate system, but with greater instrument density to resolve finer-scale age dependence. We group the Juan de Fuca and Gorda plates into ages between 0–4 Ma and >4 Ma using the magnetic lineation interpretation of Wilson (1993), comparable to age bins used for the Pacific (Nishimura & Forsyth 1988) and Indian basins (Godfrey *et al.* 2017). Due to the slow spreading rate in the Atlantic, the youngest age bin in the James *et al.* (2014) model is 0–20 Ma, while the maximum age for the Juan de Fuca and Gorda plates is 10 Ma, making comparison between these two data sets difficult.

At all periods, the Juan de Fuca plate has phase velocities faster than the Gorda plate for 0–4 Ma plate ages (Fig. 13). This is also true for plate ages > 4 Ma, but since the Juan de Fuca plate reaches maximum plate ages greater than the Gorda plate, these values are not directly comparable. Previous observations of anisotropy suggest differences beneath these two plates (Bodmer *et al.* 2015; Martin-Short *et al.* 2015) are related to variations in asthenospheric flow patterns and to varying contributions from the adjacent Pacific plate. The Gorda plate also displays extensive intraplate seismicity (Chaytor *et al.* 2004), which implies pervasive faulting that could lead to increased alteration of the lithosphere compared to Juan de Fuca. Body wave velocity and attenuation measurements (Byrnes *et al.* 2017; Eilon & Abers 2017) reinforce the idea that the Gorda plate has a distinct tectonic and structural character to the Juan de Fuca proper.

From 20 to 120 s period, average phase velocities for the 0–4 Ma age Juan de Fuca and Gorda plates are greater than found in the Pacific by Nishimura & Forsyth (1988) by ∼0.15 km s^{-1} but comparable to those found in the Indian by Godfrey *et al.* (2017) (Fig. 13b). At periods ≥80 s there is little difference between the 0–4 Ma and > 4 Ma ranges, both of which are similar to the 4–20 Ma Pacific and both Indian results. At the shortest periods (< 14 s and < 17.5 s for the Juan de Fuca and Gorda plates, respectively) the phase velocities at >4 Ma are slower than for 0–4 Ma. Lithosphere >4 Ma is adjacent to the deformation front in this system and is overlain with thicker sediment (Divins 2003; Han *et al.* 2016); thus, it is likely that the slow and thick sediment layer accounts for low phase velocities at short periods.

To further examine these age dependent phase velocity relationships, we compare our results to phase velocities predicted for lithospheric thermal models following the methods of James *et al.* (2014) and Ma & Dalton (2017). The cooling of the oceanic lithosphere is described as a function of plate age by either the half-space cooling model (HSCM) or the plate model; for the plate ages considered here, plate thickness has a negligible effect on the predictions (Stein

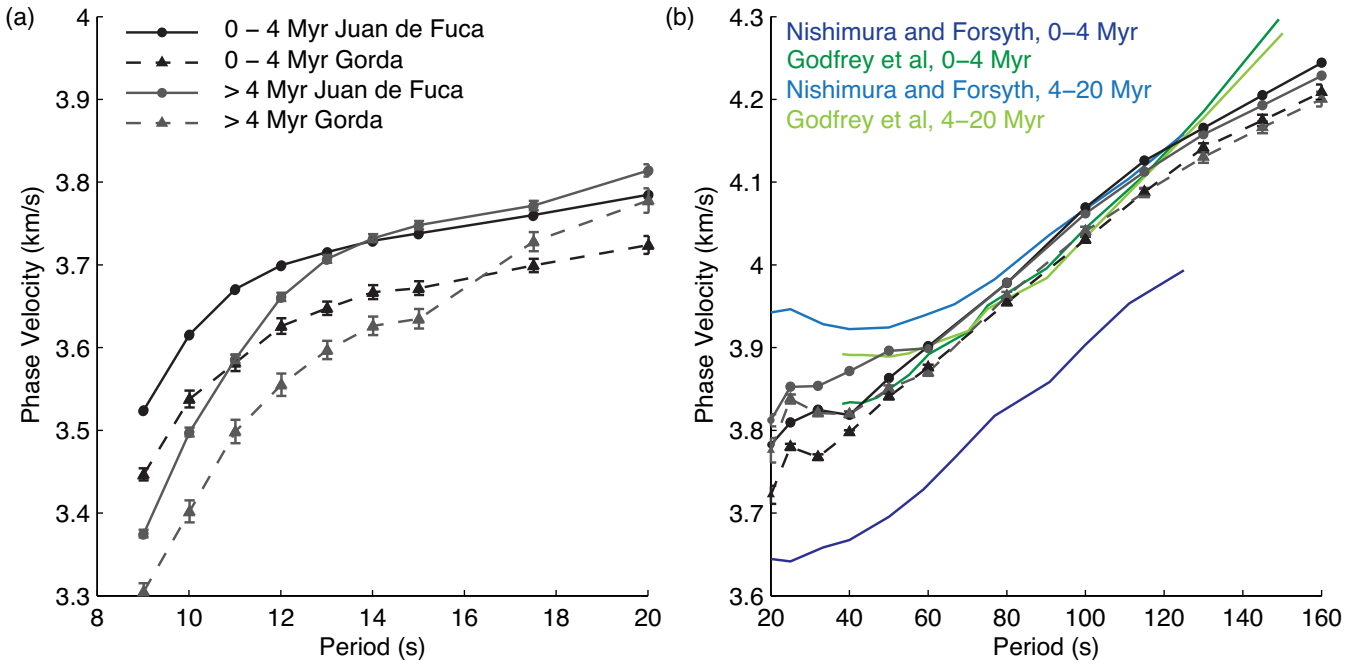

Figure 13. Phase-velocity dispersion curves for the Juan de Fuca and Gorda plates for two age ranges: 0–4 Ma and >4 Ma. (a) Results from 9 to 20 s constrained by ambient-noise data and (b) from 20 to 160 s constrained by earthquake data. Results for Pacific (Nishimura & Forsyth 1988) and Indian (Godfrey *et al.* 2017) ocean basin phase velocities are plotted for comparison.

& Stein 1992) so the HSCM is used. These models predict seafloor bathymetry and depth-dependent temperature as a function of plate age, which can be used to predict variations in seismic velocity (Jackson & Faul 2010). This framework also allows us to predict the variation in phase velocities due to changes in water depth or sediment thickness. For example, at most periods the systematic differences observed between phase velocities at 0–4 Ma in the Juan de Fuca and Gorda plates is larger than the differences predicted from variation in water depth (Ryan *et al.* 2009) and sediment thickness (Divins 2003; Supporting Information), suggesting a deeper lithospheric or asthenospheric contribution.

To investigate the effect of plate cooling, first we compare the predicted bathymetry from the HSCM to the observed bathymetry on the Juan de Fuca plate to determine the validity of using the HSCM at young ages and in the vicinity of subduction (Fig. 14); due to the small size and internal deformation of the Gorda microplate we exclude it from this analysis. Bathymetry is estimated for each grid point from the Global Multi-Resolution Topography synthesis (Ryan *et al.* 2009) using an isostatic sediment correction based on thickness from Divins (2003) except near the deformation front where higher resolution multichannel active source imaging constraints are used (Han *et al.* 2018, Fig. 1), assuming a sediment density of 2.0 g cm^{-3} following the parametrization in Ruan *et al.* (2014). We use a thermal diffusivity of 0.8047×10^{-6} m^2 s^{-1} and thermal expansion coefficient of 3×10^{-5} °C^{-1} (Stein & Stein 1992) and estimate the Juan de Fuca ridge depth as 2360 m from the median of all grid points with age < 0.25 Ma. We test mantle potential temperatures (T_p) of 1300, 1350 and 1400 °C which broadly agree with previous local studies (Hooft & Detrick 1995) and global results (Herzberg *et al.* 2007; Dalton *et al.* 2014), and overlap with values used in previous seismic studies for Cascadia (e.g. Tian *et al.* 2013; Bell *et al.* 2016; Byrnes *et al.* 2017). To first order, the HSCM can describe the observed bathymetry at seafloor ages <6 Ma for this range of mantle potential temperatures; however, older seafloor depths are systematically underpredicted even after sediment correction, probably due to subduction-related plate bending.

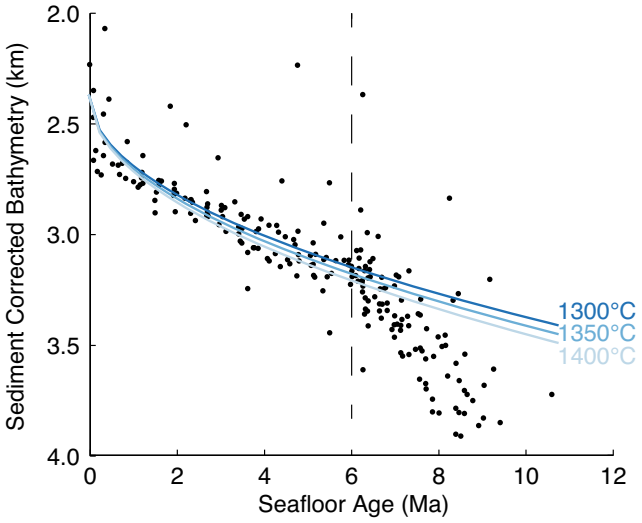

Figure 14. Sediment-corrected bathymetry for the Juan de Fuca plate as a function of seafloor age, compared with predicted bathymetry from the half-space cooling model for mantle potential temperatures of 1300, 1350 and 1400 °C. Subduction-related plate bending dominates at ages > 6 Ma.

Using this set of thermal models, we then calculate predicted seismic phase velocity for a range of assumed grain sizes. Mantle shear moduli are determined from temperature at the frequencies of observation using the empirical scaling relationships of Jackson & Faul (2010), converted to shear velocity assuming adiabatic compressibility for density (Turcotte & Schubert 1982). We use oceanic

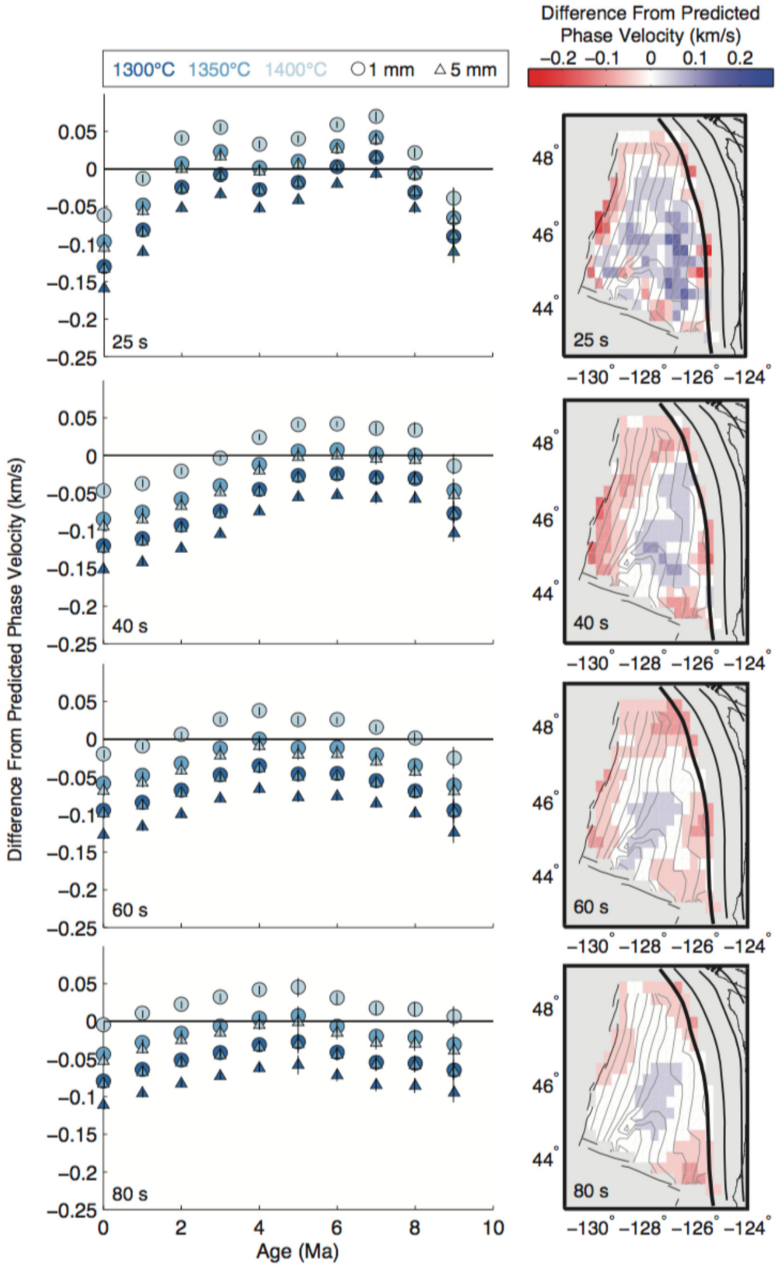

Figure 15. Comparison of predicted and observed phase velocities. Predictions are for plate cooling, taking variable water depth and sediment thickness into account. Left: the difference between predicted and observed phase velocities averaged in 1 Ma age bins for varying mantle potential temperatures (colour) and grain sizes (symbol shape); negative values indicate the observed phase velocities are slower than predicted. Uncertainty of the mean is shown as the black bar. Right: map of the difference between observed and predicted velocities using a mantle potential temperature of 1350 °C and grain size of 1 mm for the Juan de Fuca plate. Red colours indicate observed velocities are slower than predicted. Grey contours represent 1 Ma age bins (Wilson 1993). Thicker black lines same as Fig. 1.

crustal velocities from Gaherty & Dunn (2007) as an approximation for the seismic structure of the Juan de Fuca crust. Water depth and sediment thickness is specified following the same method as used for the bathymetry with sediment shear velocities parametrized as a single layer as specified in Bell *et al.* (2016). The program Mineos (Masters *et al.* 2011) is used to determine phase velocities at a given period for each grid point.

There are significant deviations between the observed phase velocities and those predicted for the HSCM on the Juan de Fuca plate (Fig. 15). While the absolute velocity values predicted by our modelling are contingent on the parameters chosen, this exercise robustly demonstrates that the velocity-age relationship is inconsistent with any purely thermal model. At ages of 0–2 Ma the velocities near the ridge are slower than predicted, and the shorter-period (25–40 s) observations cannot be explained by plausible temperature and grain-size variations. We interpret these velocities as evidence for a melt in the shallow subridge mantle, consistent with the observations from seismic attenuation (Eilon & Abers 2017), body wave tomography (Byrnes *et al.* 2017), and previous surface-wave tomography (Tian *et al.* 2013; Bell *et al.* 2016). Inferring the degree of partial melt is complicated by uncertain relationships between seismic velocity and melt fraction (e.g Eilon & Abers 2017; Byrnes

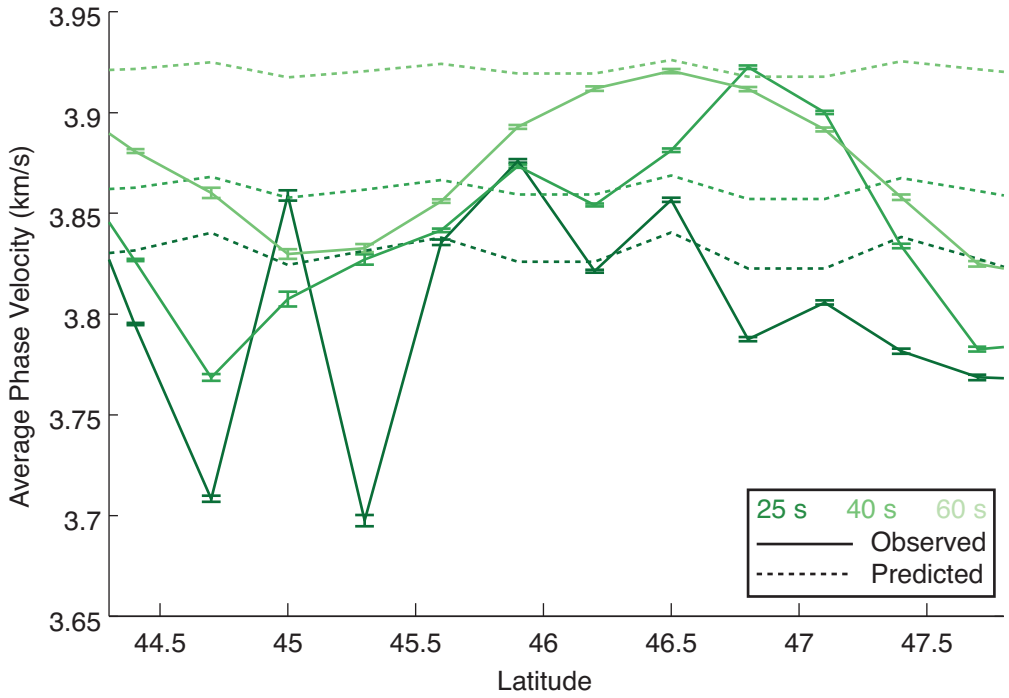

Figure 16. Average phase velocities within 75 km of the deformation front as a function of latitude for 25, 40 and 60 s (indicated by colour). Observed phase velocities are plotted as a solid line; predicted phase velocities (dashed) are estimated using the plate-cooling model with a mantle potential temperature of 1350 °C and grain size of 1 mm taking variable water depth and sediment thickness into account. Latitude range is restricted to that of the R2T line (Fig. 1) to avoid using less-resolved sediment thickness estimates near the deformation front.

et al. 2017), although our results are broadly consistent with estimates of at most 1 per cent partial melt (Hammond & Humphreys 2000) or potentially less if it coats grain boundaries (Holtzman 2016).

Away from the ridge, age-averaged velocities in the middle of the plate (3–6 Ma) suggest a relatively warm asthenosphere (T_p = 1350–1400 °C) and small grain sizes of 1–5 mm, and overall can be explained by a simple HSCM. In detail, the plate shows coherent disagreement in velocity relative to predictions from a simple cooling model (right column of Fig. 15). At 25 s period, the structure is highly heterogeneous, with substantial localized regions of relatively high velocity compared to a HSCM. At longer periods (40–80 s), the high velocities coalesce into a single coherent structure in the south-central region of the plate. At periods > 60 s, a decrease in temperature of ∼50 °C could explain the fastest phase velocities in the centre of the plate. At 25 s period, these require a larger perturbation such as ∼200 °C temperature decrease. These high-velocity regions at 25 s period may reflect crystallization removal of melt or unusually cool plate conditions induced by mantle downwelling (Bell *et al.* 2016; Byrnes *et al.* 2017). Alternatively, they may reflect more efficient cooling processes driving from the top of the plate, perhaps due to variations in sediment distribution (e.g. Divins 2003; Han *et al.* 2016), water penetration or cooling associated with propagator wakes and other pre-existing fabric (e.g. Han *et al.* 2016; Horning *et al.* 2016). While the peak depth sensitivities for these periods are expected within the mantle (Fig. 12), variations in shallow structure alone can affect predicted phase velocities at these periods (Supporting Information) suggesting that these top-down processes may likely play a role in the observed variations. Regardless, the observations suggest that the thermal structure of the plate deviates from half-space cooling, particularly at the shortest periods. Once subducted, this heterogeneity may induce variations in seismogenic and/or magmatic processes along strike, for example, by regulating the extent to which the incoming plate is hydrated.

Phase velocities at the oldest crust (7–9 Ma) near the deformation front are slower than those observed seawards in the centre of the plate (Fig. 8), and highly variable along the margin. This is in part driven by thickening sediment near the margin, but variability remains even after taking that into account. We compare the observed phase velocities with those predicted for plate cooling, and variable water depth and sediment thicknesses near the deformation front (Fig. 16). While there is uncertainty in the accuracy of these plate cooling models near the deformation front given the heterogeneity observed in the centre of the plate, the models should reflect expected along-margin variations in phase velocity due to age, water depth, and sediment variations, particularly where sediment thickness is constrained by coincident MCS data (Han *et al.* 2018). The observed range of phase velocities at periods of 25, 40 and 60 s is approximately five times the predicted range, indicating that the observed variation is not solely due to local variations in water depth and sediment thickness. Notably, relatively slow phase velocities at short periods (e.g. 25 s) exist south of 45.5 °N. This corresponds with an observed southward reduction of compressional seismic velocities in the lower crust and inferred elevated hydration (Canales *et al.* 2017), and with more extensive subduction-related bending faults that transect the crust (Han *et al.* 2016; Han *et al.* 2018). Furthermore, a propagator wake associated with past ridge migration (e.g. Nedimovic *et al.* 2009) is also located in this region, which has been identified using active-source imaging as a region of relatively elevated lower-crustal and mantle hydration (Han *et al.* 2016; Horning *et al.* 2016; Canales *et al.* 2017). Taken together, these observations suggest that slow phase velocities south of 45.5 °N are correlated with locations of increased crustal and mantle hydration and may have a related source. While the expected peak

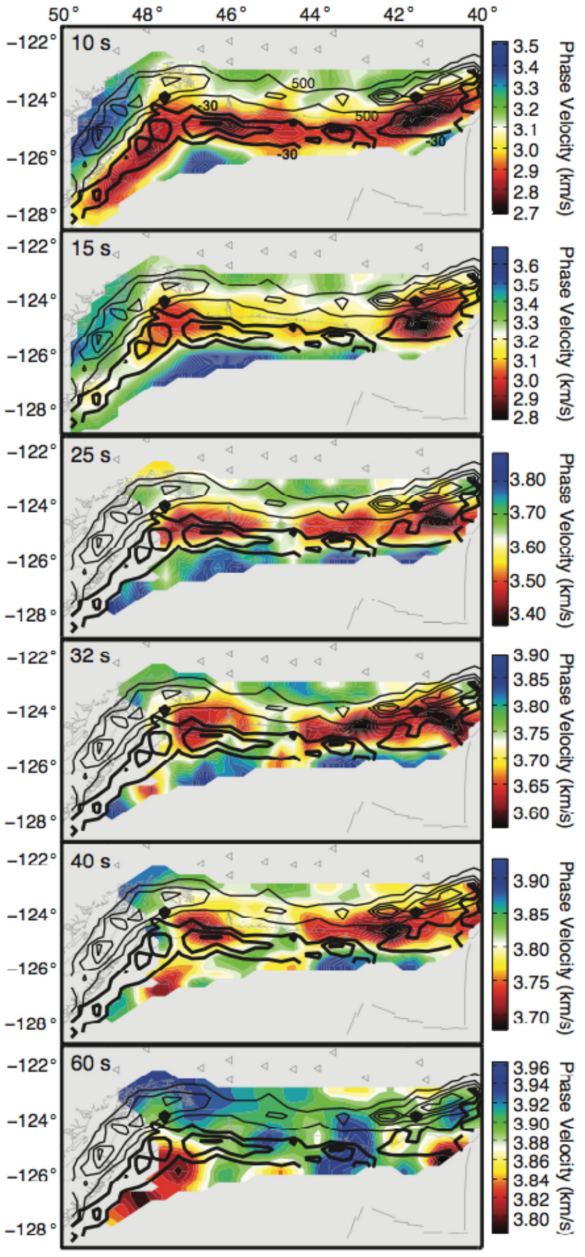

Figure 17. Phase velocities in the forearc region, extending from the deformation front to the 60-km-depth contour of the slab (McCrory *et al.* 2012). Thick black lines are negative isostatic gravity anomaly contours (Bonvalot *et al.* 2012). Thin black lines are contours of number of tremor events per 0.3°-spaced grid cell from 2009 August 6 to 2017 August 28 (Wech 2010) (https://pnsn.org/tremor). The gravity anomaly contours correspond to −30, −50 and −70 mGal. Tremor contours correspond to 500, 2500, 5000 and 7500 recorded events. Panels are oriented with northwards towards the left.

depth sensitivities of our periods are deeper than the crust and upper mantle, the kernels are broad and have sensitivity to shallow lithosphere structure. Resolution tests show that these variations do not result from lateral smearing from the slow velocities on the adjacent shelf (Supporting Information).

It is possible that the anomalously slow velocities at plate ages >6 Ma reflect anomalous thermal processes in the asthenosphere, in addition to the topdown processes such as hydration. This is particularly true for observations at the longest periods (≥80 s), which are difficult to attribute to structure in the crust and uppermost mantle. Rather, these data suggest relatively high mantle temperatures in parts of the Juan de Fuca region (Fig. 15). Hawley *et al.* (2016) use body wave data to argue for a broad, along-strike, low-velocity zone in the asthenosphere beneath the Cascadia outer rise and forearc. Bodmer *et al.* (2018) similarly observe a low-velocity asthenosphere, but it is largely restricted to the northern and southern regions of the margin. The anomalies in our phase velocity models weaken at longer periods (especially the anomaly at 45–46°N) and are not present continuously along the deformation front. It is possible that a deeper anomaly contributes to these deviations; however, this process likely offers a secondary contribution to the plate-cooling deviation compared to the inferred hydration process discussed above. A combination of both effects may also help explain why these anomalies appear strongest closer to the deformation front rather than in the centre of the plate.

4.2 The forearc of the Cascadia subduction zone

The transition from oceanic crust to the accretionary wedge results in a sharp decrease in phase velocities eastwards of the deformation front at periods ≤ 40 s (Fig. 8). At 10–15 s period this region contains the slowest phase velocities in the entire study area. Predicted sensitivity kernels suggest that the depth sensitivity is strongly peaked in the upper crust for short periods in the accretionary wedge (10–20 s; Fig. 11). Moving eastwards, velocities increase as the accretionary wedge transitions to more typical continental crust until reaching the volcanic arc. We interpret the variation of short to mid-band phase velocities in the forearc by comparing them with gravity anomalies and seismogenic properties. Resolution tests (Supporting Information) indicate features are well resolved in the entire forearc at dimensions of at least 100 km for periods of 20–80 s, and onshore at periods of 10–15 s. Some smearing exists at these scales for the offshore forearc at 10–15 s and ≥ 80 s periods, but features at the scale of 130 km are well resolved.

From 10 to 15 s, phase velocities are slowest within the region of observed offshore negative isostatic gravity anomalies (Bonvalot *et al.* 2012; Fig. 17). These gravity anomalies spatially coincide with large sedimentary basins (Wells *et al.* 2003), as well as asperities of past megathrust ruptures estimated from coastal subsidence (Wang *et al.* 2013). Exceptionally slow phase velocities are observed spanning the coastline (Fig. 17) in the vicinity of the Olympic Peninsula (47–48.5°N), and just north of the Mendocino Triple Junction (near 41°N), consistent with previous seismic observations (Porritt *et al.* 2011; Calkins *et al.* 2011; Gao 2016). These slow features also approximately coincide with the along-strike location of low-velocity zones interpreted as widespread hydration of the subducting mantle from offshore surface-wave imaging (Bell *et al.* 2016). Given the strength of the anomalies at the shortest periods (10–15 s) and the shallow sensitivity of these periods in forearc crust (Fig. 11), we interpret the slow velocities as reflective of basin and upper-crustal structure that may relate to significant slip in previous megathrust earthquakes. If hydrated mantle in the underlying slab is spatially coincident with these features, then it is a secondary contribution to the slow phase velocities.

Slow velocities are also observed in similar locations at 25–40 s period, although they are slightly landward of those observed from 10 to 15 s. Eastwards, the Cascadia forearc transitions from an accretionary prism over the megathrust locked zone (Goldfinger *et al.* 2012; Wang *et al.* 2013) to forearc crust overlying a plate interface characterized by episodic tremor and slip (ETS) and, primarily

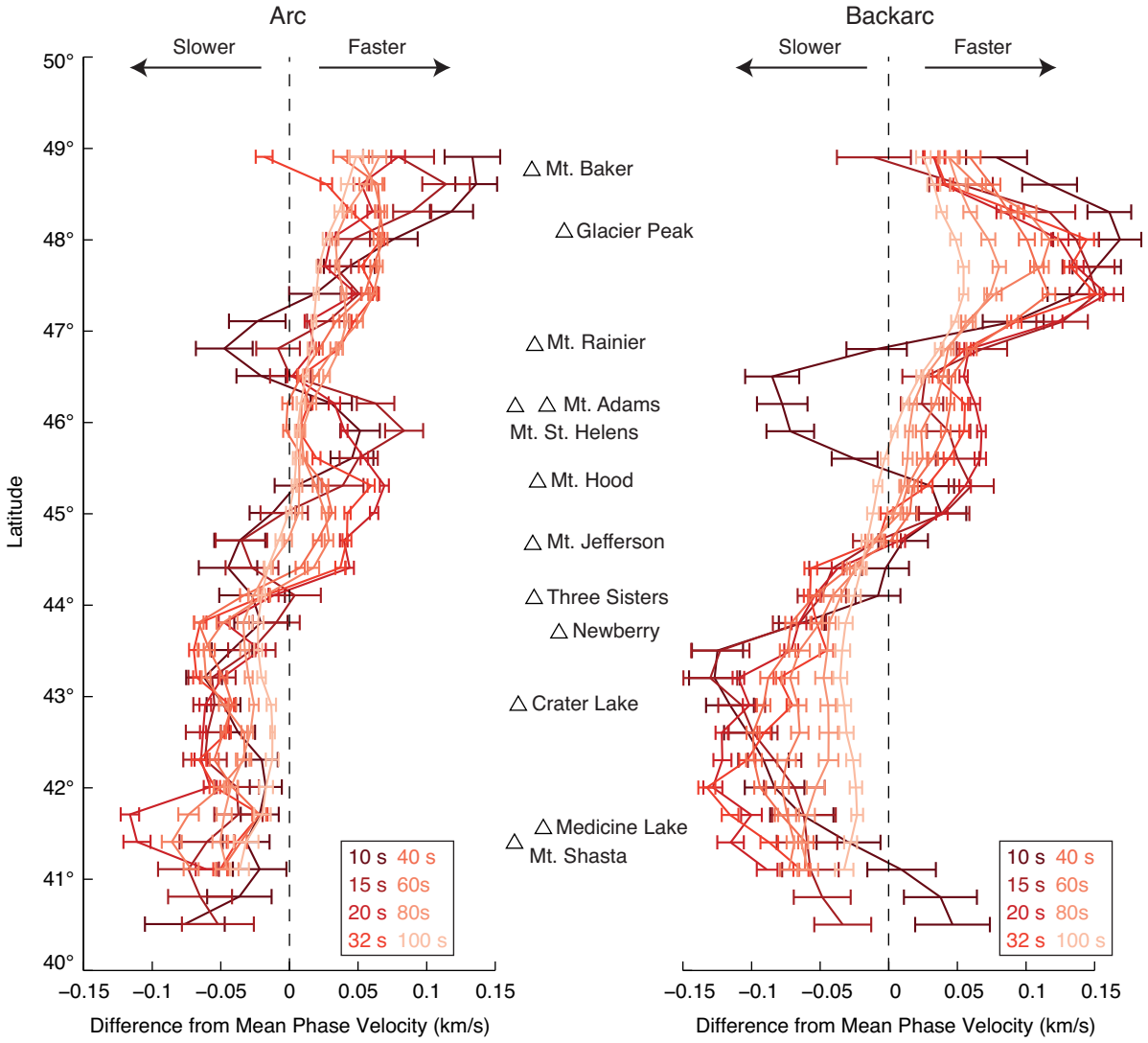

Figure 18. Differences from the mean phase velocity along the volcanic arc (left) and backarc (right) as a function of latitude. For each latitude grid cell an average phase velocity is calculated for longitude values within the specified range (Fig. 1, arc and backarc boxes). These are then differenced from the mean value for the entire volcanic arc at each period. Negative differences imply the phase velocities are slower than average for the entire arc, whereas positive values indicate faster velocities. The locations of the Cascades volcanoes are plotted for reference.

beneath the Olympic peninsula and Mendocino Triple Junction, intraslab earthquakes (McCrory *et al.* 2012). ETS events in Cascadia occur along the plate interface between depths of ∼30 and 40 km (Ghosh *et al.* 2009) and may be related to elevated pore fluid pressures along the plate interface (Audet *et al.* 2009; Houston 2015; Gao & Wang 2017), whereas intraslab earthquakes in Cascadia occur below the subducting Moho related to metamorphic dehydration reactions (Abers *et al.* 2013). One outstanding question is whether the occurrence of episodic tremor and slip is primarily modulated by variations in the structure of the subducting crust or the overriding continental crust. The location of ETS is consistently landward of the slowest phase velocities at 25–40 s period in the forearc (Fig. 17). The regions of highest density and most frequent tremor (Boyarko *et al.* 2015), as well as the locations of intraslab earthquakes (McCrory *et al.* 2012), are approximately directly downdip from the slow velocities observed along the coastline near the Olympic Peninsula and Mendocino Triple Junction, while low tremor density and absence of intraslab earthquakes are seen near 46°N where forearc velocities are locally highest at these periods. There is also evidence of variations in the geology of the overriding crust along the strike of the forearc (e.g. Brudzinski & Allen 2007; Wells *et al.* 2017) that may contribute to the observed variations. However, the spatial offset between the correlation of phase velocities and seismic behavior suggests that a compositional or thermal transition from slow (weak) to fast (stronger) overriding crust may delineate the updip extent of tremor. The relationship with intraslab seismicity additionally supports that both observations may have a common cause such as variations in fluid release/retention along the megathrust, perhaps also related to variations in underthrusting sediment (Delph *et al.* 2018).

4.3 The Cascades volcanic arc

Slow phase velocities are associated with the Cascades volcanic arc at all periods; at shorter periods these are primarily located directly

beneath the trend of volcanoes, while at longer periods the slowest velocities extend several hundred kilometers into the backarc, particularly in the south. Although slow velocities extend southeast in the backarc at 10 s period (Fig. 8), this is in a region of reduced resolution. The backarc is well constrained in the earthquake phase velocity maps due to the inclusion of Transportable Array data from 2006 to 2008; therefore, the southeast region at periods $\geq$ 20 s is robust (Supporting Information).

Along-arc variations of these phase velocities beneath the arc and in the backarc (Fig. 18) broadly agree with previous seismic phase velocity observations (Wagner *et al.* 2010; Porritt *et al.* 2011; Lin & Ritzwoller 2011; Jin & Gaherty 2015), although the better-resolution amphibious data yield velocity anomalies that are more localized along the arc. Phase velocities at all periods are slowest in the southern Cascades, from Mt. Shasta (41°N) northward to Three Sisters (44°N). In contrast, relatively high phase velocities exist beneath the arc and backarc near the two northernmost arc volcanoes, Glacier Peak (48°N) and Mt. Baker (49°N).

The along-arc variations in phase velocity correlate with trends in the extrusive magmatic productivity of the Cascades arc, with lower volumes in the north and higher volumes in the south (Sherrod & Smith 1990; Hildreth 2007). Similar patterns are observed in surface heat flow measurements (Ingebritsen & Mariner 2010), with higher heat flow in the southern Cascades. These correlations are identified and analysed by Till *et al.* (2019), who show that quantitative agreement exists between our 10–60 s phase velocities and average surface heat flow, erupted volcanic volumes, and the petrologically estimated magmatic heat budget along the entire Cascades arc. These correlations are strongest from 20 to 60 s, the period range primarily sensitive to lower crustal and upper-mantle structure. This observation suggests that heat input from magma input in the lower crust and upper mantle associated with extrusive volcanism drives the heating throughout the arc crust. The correlation at 40–60 s implies that the variation in temperature and perhaps melt content extends into the mantle wedge supporting vertically connected arc magmatism, with higher extents of heating and/or melt content in the southern Cascades (Till *et al.* 2019). At periods longer than 60 s, where peak sensitivities are at >100 km depth, these data sets are more weakly correlated. At these periods, phase velocities evidently become increasingly dominated by structure below the melt production region, offering a weak constraint on the base of arc melting.

5 CONCLUSIONS

We have imaged the Cascadia subduction zone from the ridge through the volcanic arc using Rayleigh waves, resulting in shoreline-crossing phase-velocity maps from 9 to 160 s. The OBS data were systematically corrected for tilt and compliance noise using an automated quality-control procedure to calculate high-quality transfer functions. We are able to robustly image tectonic features associated with the subduction system both offshore and onshore including the transition from oceanic to continental lithosphere, the Juan de Fuca and Gorda ridges, the slow accretionary forearc and the volcanic arc.

Within the oceanic plate prior to subduction we observe that the Gorda plate has systematically slower phase velocities than the Juan de Fuca plate at all periods that likely reflects widespread differences in lithospheric or asthenospheric structure. The Juan de Fuca plate phase velocities cannot be explained by thermal variations alone and likely require some melt beneath the ridge, and while they coarsely agree with conductive plate cooling predictions, significant deviations from half-space cooling are evident within the center of the plate. Regions of slow phase velocities are observed just outboard of the deformation front, coincident with similar observations from active-source data indicative of increased faulting and crustal and upper-mantle hydration. Within the forearc, regions of slow velocities from 10 to 15 s near the coastline are coincident with gravity lows inferred to be forearc basins and overlap with modelled regions of high slip in past megathrust earthquakes. These slow-velocity regions tend to shift slightly landward from 25 to 40 s period suggesting a depth-varying source. In addition, these slow velocities tend to lie directly updip of regions with most abundant tremor and intraslab seismicity, indicating a relationship between velocity structures and tectonic phenomena that persist significantly downdip; we suggest these are both driven by the hydration extent of the downgoing plate. Finally, the volcanic arc and backarc display significant along-strike variations in velocity, correlated with a southward increase in magmatic productivity and accompanying crustal heating. Overall, the amphibious phase-velocity maps yield a complete image of the lithosphere of the Cascadia margin, highlighting relationships between water, temperature, seismicity and magma productivity along the subduction zone.

SUPPORTING INFORMATION

Supplementary data are available at *GJI* online.

Figure S1. Phase-velocity maps derived from ambient-noise data. The period is indicated in the lower left corner of each map. Colours represent phase velocities in km s^{-1}, with individual scales for each map.

Figure S2. Uncertainty maps for ambient-noise phase velocities derived from bootstrapping. The period is indicated in the lower left corner of each map. Colours represent phase-velocity standard deviation in km s^{-1}.

Figure S3. Cross-correlation paths between stations used for the ambient-noise phase-velocity map inversion at each period.

Figure S4. Checkerboard test for ambient-noise data using checkers spaced on a 100 km grid. The period is indicated in the lower left corner of each map. Colours represent phase velocity in km s^{-1}.

Figure S5. Checkerboard test for ambient-noise data using checkers spaced on a 130 km grid. The period is indicated in the lower left corner of each map. Colours represent phase velocity in km s^{-1}.

Figure S6. Phase-velocity maps derived from earthquake surface-wave data. The period is indicated in the lower left corner of each map. Colours represent phase velocities in km s^{-1}, with individual scales for each map. These phase-velocity maps are the results derived from the Helmholtz equation.

Figure S7. Phase-velocity standard deviation maps for earthquake surface-wave data. The period is indicated in the lower left corner of each map. Colours represent standard deviations of the mean in km s^{-1}.

Figure S8. Ray-path density maps for earthquake surface-wave data. The period is indicated in the lower left corner of each map. Colours represent number of ray paths, with the scale saturated for values larger than 10 000 to account for the variations in deployment time.

Figure S9. Phase-velocity maps derived from earthquake surface-wave data using the Eikonal equation. These results have

not been corrected for focusing and defocusing, and are presented for comparison to the final Helmholtz result. The period is indicated in the lower left corner of each map. Colours represent phase velocities in km s^{-1}, with individual scales for each map.

Figure S10. Checkerboard test for the phase-velocity map using a 100 km grid. The period is indicated in the lower left corner of each map. We estimate these by calculating checkerboard tests with the Eikonal equation for each individual earthquake, and then stacking the results. They do not reflect any resolution constraints related to the amplitude information used in the Helmholtz result, but provide an estimate of the resolution of the time information.

Figure S11. Checkerboard test for the phase-velocity result using a 130 km grid. The period is indicated in the lower left corner of each map. We estimate these by calculating checkerboard tests with the Eikonal equation for each individual earthquake, and then stacking the results. They do not reflect any resolution constraints related to the amplitude information used in the Helmholtz result, but provide an estimate of the resolution of the time information.

Figure S12. Resolution testing for a slow-velocity strip at the forearc. The top right panel is the input velocity model; output periods are indicated in the lower left corner of each panel. The slowest velocities are input where the offshore elevation is shallower than 750 m, extending onshore up until the 20 km slab depth contour to approximate the shelf and coastal sediments.

Figure S13. Comparison of ambient-noise cross-correlation functions for the OBS G30A (black) and G30B (red) filtered from 8 to 25 s with common station pairs. These two stations reoccupied the same site in two different deployment years and produce similar cross-correlation functions for station pairs they have in common with each other.

Figure S14. Difference in average phase velocity between 0 and 4 Ma ages on the Juan de Fuca and Gorda plates. The dashed line indicates the observed differences in the phase-velocity curve, while the solid line indicates the predicted differences taking water depth and sediment thickness into account. At all periods, except 25 s, the difference observed is larger than the predicted difference, suggesting structural differences in the lithosphere or underlying asthenosphere as the cause rather than shallow structures.

Figure S15. Predicted phase-velocity curves for an oceanic plate that is 3 Ma with $T_p = 1350$ °C and grain size of 1 mm for a suite of water depths and sediment thicknesses.Seismic Earth: Array Analysis of Broadband Seismograms

Table S1. Processing of OBS prior to Helmholtz phase-velocity calculation.

Please note: Oxford University Press are not responsible for the content or functionality of any supporting materials supplied by the authors. Any queries (other than missing material) should be directed to the corresponding author for the paper.

ACKNOWLEDGEMENTS

We thank the members of the Cascadia Initiative Expedition Team for their efforts. The offshore data used in this research were provided by instruments from the Ocean Bottom Seismograph Instrument Pool (http://www.obsip.org). All seismic data used in this paper are archived at the Incorporated Research Institutions for Seismology (IRIS) Data Management Center (http://www.iris.edu). We thank Zhitu Ma for sharing computer codes used in this study, Spahr Webb for providing valuable insights into OBS noise, Sam Bell, Ge Jin, Rob Porritt and Lara Wagner for sharing phase-velocity maps and Shuoshuo Han for sharing sediment-thickness profiles. We thank Songqiao Wei and Doug Toomey for their insightful reviews that helped to improve this manuscript. This work is funded by National Science Foundation Award Number OCE-1334831 and is based upon work supported by the National Science Foundation Graduate Research Fellowship under Grant Number DGE-11-44155.

REFERENCES

Abers, G.A., MacKenzie, L.S., Rondenay, S., Zhang, Z., Wech, A.G. & Creager, K.C., 2009. Imaging the source region of Cascadia tremor and intermediate-depth earthquakes, *Geology,* **37**(12), 1119–1122.

Abers, G.A., Nakajima, J., van Keken, P.E., Kita, S. & Hacker, B.R., 2013. Thermal-petrological controls on the location of earthquakes within subducting plates, *Earth planet. Sci. Lett.,* **369–370,** 178–187.

Accardo, N.J. *et al.*, 2017. Surface wave imaging of the weakly extended Malawi Rift from ambient-noise and teleseismic Rayleigh waves from onshore and lake-bottom seismometers, *Geophys J. Int.,* **209**(3), 1892–1905.

Aki, K., 1957. Space and time spectra of stationary stochastic waves, with special reference to microtremors, *Bull. Earthq. Res. Inst.,* **35,** 415–457.

Audet, P., Bostock, M.G., Christensin, N.I. & Peacock, S.M., 2009. Seismic evidence for overpressured subducted oceanic crust and megathrust fault sealing, *Nature,* **457,** 76–78.

Bell, S., Ruan, Y. & Forsyth, D.W., 2016. Ridge asymmetry and deep aqueous alteration at the trench observed from Rayleigh wave tomography of the Juan de Fuca plate, *J. geophys. Res.,* **121,** 7298–7321.

Bell, S.W., Forsyth, D.W. & Ruan, Y., 2014. Removing noise from the vertical component records of ocean-bottom seismometers: results from year one of the Cascadia Initiative, *Bull. seism. Soc. Am.,* **105,** 300–313.

Bell, S.W., Ruan, Y. & Forsyth, D.W., 2015. Shear velocity structure of abyssal plain sediments in Cascadia, *Seismol. Res. Lett.,* **86**(5), 1247–1252.

Bodmer, M., Toomey, D.R., Hooft, E.E., Nábělek, J. & Braunmiller, J., 2015. Seismic anisotropy beneath the Juan de Fuca plate system: evidence for heterogeneous mantle flow, *Geology,* **G37181,** 1–5.

Bodmer, M., Toomey, D.R., Hooft, E.E.E. & Schmandt, B., 2018. Buoyant asthenosphere beneath Cascadia influences megathrust segmentation, *Geophys. Res. Lett.,* **45,** 6954–6962.

Bonvalot, S. *et al.*, 2012. World Gravity Map, Commission for the Geological Map of the World, Eds. BGI-CGMW-CNES-IRD, Paris.

Bowden, D.C., Kohler, M.D., Tsai, V.C. & Weeraratne, D.S., 2016. Offshore Southern California lithospheric velocity structure from noise cross-correlation functions, *J. geophys. Res.,* **121**, 3415–3427.

Boyarko, D., Brudzinski, M., Porritt, R., Allen, R. & Tréhu, A., 2015. Automated detection and location of tectonic tremor along the entire Cascadia margin from 2005 to 2011, *Earth planet. Sci. Lett.,* **430,** 160–170.

Brocher, T.M., 2005. Empirical relations between elastic wavespeeds and density in the Earth's crust, *Bull. seism. Soc. Am.,* **95**(6), 2081–2092.

Brudzinski, M.R. & Allen, R.M., 2007. Segmentation in episodic tremor and slip all along Cascadia, *Geology,* **35**(10), 907–910.

Byrnes, J.S., Toomey, D.R., Hooft, E.E.E., Nábělek, J. & Braunmiller, J., 2017. Mantle dynamics beneath the discrete and diffuse plate boundaries of the Juan de Fuca plate: results from Cascadia Initiative body wave tomography, *Geochem. Geophys. Geosyst.,* **15**(B10), 3521–3524.

Calkins, J.A., Abers, G.A., Ekstro¨m, G., Creager, K.C. & Rondenay, S., 2011. Shallow structure of the Cascadia subduction zone beneath western Washington from spectral ambient noise correlation, *J. geophys. Res.,* **116,** B07302, doi:10.1029/2010JB007657.

Canales, J.P., Carbotte, S.M., Nedimović, M.R. & Carton, H., 2017. Dry Juan de Fuca slab revealed by quantification of water entering Cascadia subduction zone, *Nat. Geosci.,* **10**(11), 864–870.

Castagna, J.P., Batzle, M.L. & Eastwood, R.L., 1985. Relationships between compressional-wave and shear-wave velocities in clastic silicate rocks, *Geophysics,* **50,** 571–581.

Chaytor, J.D., Goldfinger, C., Dziak, R.P. & Fox, C.G., 2004. Active deformation of the Gorda plate: constraining deformation models with new geophysical data, *Geology,* **32,** 353–356.

Crawford, W.C. & Webb, S.C., 2000. Identifying and removing tilt noise from low-frequency (<0.1 Hz) seafloor vertical seismic data, *Bull. seism. Soc. Am.,* **90,** 952–963.

Crosbie, K., 2018. Shear velocity structure from ambient noise and teleseismic surface wave tomography in the Cascades around Mt. St. Helens, *MS dissertation*, Cornell University.

Dalton, C.A., Langmuir, C.H. & Gale, A., 2014. Geophysical and geochemical evidence for deep temperature variations beneath mid- ocean ridges, *Science,* **344**(6179), 80–83.

Delph, J.R., Levander, A. & Niu, F., 2018. Fluid controls on the heterogeneous seismic characteristics of the Cascadia margin, *Geophys. Res. Lett.,* **45**(20), 11 021–11 029.

DeMets, C., Gordon, R.G. & Argus, D.F., 2010. Geologically current plate motions, *Geophys. J. Int.,* **181**(1), 1–80.

Divins, D.L., 2003. *Total Sediment Thickness of the World's Oceans & Marginal Seas,* NOAA Natl. Geophys. Data Cent.

Eilon, Z.C. & Abers, G.A., 2017. High seismic attenuation at a mid-ocean ridge reveals the distribution of deep melt, *Sci. Adv.,* **3**(5), e1602829, doi:10.1126/sciadv.1602829.

Ekström, G., Abers, G.A. & Webb, S.C., 2009. Determination of surface-wave phase velocities across USArray from noise and Aki's spectral formulation, *Geophys. Res. Lett.,* **36,** L18301, doi:10.1029/2009GL039131.

Forsyth, D.W. & Li, A., 2005. Array-analysis of two-dimensional variations in surface wave phase velocity and azimuthal anisotropy in the presence of multipathing interference, in *Seismic Earth: Array Analysis of Broadband Seismograms,* pp. 81–98, eds Levander, A. & Nolet, G., AGU.

Foster, A., Ekström, G. & Nettles, M., 2014. Surface wave phase velocities of the western United States from a two-station method, *Geophys. J. Int.,* **196**(2), 1189–1206.

French, S., Lekic, V. & Romanowicz, B., 2013. Waveform tomography reveals channeled flow at the base of the oceanic asthenosphere, *Science,* **342,** 6155.

Gaherty, J.B. & Dunn, R.A., 2007. Evaluating hot spot–ridge interaction in the Atlantic from regional-scale seismic observations, *Geochem. Geophys. Geosyst.,* **8,** Q05006, doi:10.1029/2006GC001533.

Gao, H., 2016. Seismic velocity structure of the Juan de Fuca and Gorda plates revealed by a joint inversion of ambient noise and regional earthquakes, *Geophys. Res. Lett.,* **43**(10), 5194–5201.

Gao, H., 2018. Three-dimensional variation of the slab geometry correlate with earthquake distributions at the Cascadia subduction system, *Nat. Commun.,* doi:10.1038/s41467-018-03655-5.

Gao, H. & Shen, Y., 2015. A preliminary full-wave ambient noise tomography model spanning from the Juan de Fuca and Gorda spreading centers to the Cascadia volcanic arc, *Seismol. Res. Lett.,* **86**(5), doi:10.1785/0220150103.

Gao, X. & Wang, K., 2017. Rheological separation of the megathrust seismogenic zone and episodic tremor and Slip, *Nature,* **543,** 416–419.

Ghosh, A., Vidale, J.E., Sweet, J.R., Creager, K.C. & Wech, A.G., 2009. Tremor patches in Cascadia revealed by seismic array analysis, *Geophys. Res. Lett.,* **36,** L17316, doi:10.1029/2009GL039080.

Godfrey, K.E., Dalton, C.A. & Ritsema, J., 2017. Seafloor age dependence of Rayleigh wave phase velocities in the Indian Ocean, *Geochem. Geophys. Geosyst.,* **18**(5), 1926–1942.

Goldfinger, C. *et al.*, 2012. Turbidite event history: methods and implications for Holocene paleoseismicity of the Cascadia subduction zone, pp. 184, United States Geological Survey Professional Paper 1661-F.

Hammond, W.C. & Humphreys, E.D., 2000. Upper mantle seismic wave velocity: effects of realistic partial melt geometries, *J. geophys. Res.,* **105**(B5), 10 975–10 986.

Han, S., Carbotte, S.M., Canales, J.P., Nedimovic´, M.R., Carton, H., Gibson, J.C. & Horning, G.W., 2016. Seismic reflection imaging of the Juan de Fuca plate from ridge to trench: New constraints on fault evolution and crustal structure prior to subduction, *J. geophys. Res.,* **121,** 1849–1872.

Han, S., Carbotte, S.M., Canales, J.P., Nedimović, M.R. & Carton, H., 2018. Along-Trench structural variations of the subducting Juan de Fuca plate from multichannel seismic reflection imaging, *J. geophys. Res.,* **11**(3), 465–25.

Harmon, N., Forsyth, D. & Webb, S., 2007. Using ambient seismic noise to determine short-period phase velocities and shallow shear velocities in young oceanic lithosphere, *Bull. seism. Soc. Am.,* **97**(6), 2009–2023.

Hawley, W.B., Allen, R.M. & Richards, M.A., 2016. Tomography reveals buoyant asthenosphere accumulating beneath the Juan de Fuca plate, *Science,* **353**(6306), 1406–1408.

Herrmann, R.B., 2013. Computer programs in seismology: an evolving tool for instruction and research, *Seismol. Res. Lett.,* **84**(6), 1081–1088.

Herrmann, R.B. & Ammon, C.J., 2004. *Computer Programs in Seismology: Surface Waves, Receiver Functions, and Crustal Structure,* version 3.30, St. Louis University.

Herzberg, C., Asimow, P.D., Arndt, N., Niu, Y., Lesher, C.M., Fitton, J.G., Cheadle, M.J. & Saunders, A.D., 2007. Temperatures in ambient mantle and plumes: Constraints from basalts, picrites, and komatiites, *Geochem. Geophys. Geosyst.,* **8,** Q02006, doi:10.1029/2006GC001390.

Hildreth, W., 2007. Quaternary magmatism in the Cascades—geologic perspectives, United States Geological Survey Professional Paper 1744, pp. 125.

Holtzman, B.K., 2016. Questions on the existence, persistence, and mechanical effects of a very small melt fraction in the asthenosphere, *Geochem. Geophys. Geosyst.,* **17,** 470–484.

Hooft, E.E.E. & Detrick, R.S., 1995. Relationship between axial morphology, crustal thickness, and mantle temperature along the Juan de Fuca and Gorda ridges, *J. geophys. Res.,* **100**(B11), 22 499–22 508.

Horning, G., Canales, J.P., Carbotte, S.M., Han, S., Carton, H., Nedimovic´, M.R. & van Keken, P.E., 2016. A 2-D tomographic model of the Juan de Fuca plate from accretion at axial seamount to subduction at the Cascadia margin from an active source ocean bottom seismometer survey, *J. geophys. Res.,* 121, doi:10.1002/2016JB013228.

Houston, H., 2015. Low friction and fault weakening revealed by rising sensitivity of tremor to tidal stress, *Nat. Geosci.,* **8,** 409–415.

Ingebritsen, S.E. & Mariner, R.H., 2010. Hydrothermal heat discharge in the Cascade Range, northwestern United States, *J. Volc. Geotherm. Res.,* **196**(3-4), 208–218.

Jackson, I. & Faul, U.H., 2010. Grainsize-sensitive viscoelastic relaxation in olivine: Towards a robust laboratory-based model for seismological application, *Phys. Earth planet. Inter.,* **183**(1), 151–163.

James, E.K., Dalton, C.A. & Gaherty, J.B., 2014. Rayleigh wave phase velocities in the Atlantic upper mantle, *Geochem. Geophys. Geosyst.,* **15**(11), 4305–4324.

Janiszewski, H.A. & Abers, G.A., 2015. Imaging the plate interface in the Cascadia seismogenic zone: new constraints from offshore receiver functions, *Seismol. Res. Lett.,* **86**(5), 1261–1269.

Jin, G. & Gaherty, J.B., 2015. Surface wave phase-velocity tomography based on multichannel cross-correlation, *Geophys. J. Int.,* **201,** 1383–1398.

Jin, G., Gaherty, J.B., Abers, G.A., Kim, Y., Eilon, Z. & Buck, W.R., 2015. Crust and upper mantle structure associated with extension in the Woodlark Rift, Papua New Guinea from Rayleigh-wave tomography, *Geochem. Geophys. Geosyst.,* **16**(11), 3808–3824.

Kustowski, B., Ekström, G. & Dziewonski, A.M., 2008. Anisotropic shear-wave velocity structure of the Earth's mantle: a global model, *J. geophys. Res.,* **113,** B06306, doi:10.1029/2007JB005169.

Li, J., Shillington, D.J., Bécel, A., Nedimović, M.R., Webb, S.C., Saffer, D.M., Keranen, K.M. & Kuehn, H., 2015. Downdip variations in seismic reflection character: Implications for fault structure and seismogenic behavior in the Alaska subduction zone, *J. geophys. Res.,* **120**(11), 7883–7904.

Lin, F.-C. & Ritzwoller, M.H., 2010. Empirically determined finite frequency sensitivity kernels for surface waves, *Geophys. J. Int.,* **182**(2), 923–932.

Lin, F.-C. & Ritzwoller, M.H., 2011. Helmholtz surface wave tomography for isotropic and azimuthally anisotropic structure, *Geophys. J. Int.,* **186**(3), 1104–1120.

Lin, F.-C., Ritzwoller, M.H. & Snieder, R., 2009. Eikonal tomography: surface wave tomography by phase front tracking across a regional broadband seismic array, *Geophys. J. Int.,* **177,** 1091–1110.

Martin-Short, R., Allen, R.M., Bastow, I.D., Totten, E. & Richards, M.A., 2015. Mantle flow geometry from ridge to trench beneath the Gorda–Juan de Fuca plate system, *Nat. Geosci.,* **8**(12), 965–968.

Masters, G., Woodhouse, J.H. & Freeman, G., 2011. Mineos v1.0.2 [software], Computational Infrastructure for Geodynamics, https://geodynamics.org/cig/software/mineos/.

Ma, Z. & Dalton, C.A., 2017. Evolution of the lithosphere in the Indian Ocean from combined earthquake and ambient noise tomography, *J. geophys. Res.,* **122**(1), 354–371.

McCrory, P.A., Blair, J.L., Waldhauser, F. & Oppenheimer, D.H., 2012. Juan de Fuca slab geometry and its relation to Wadati– Benioff zone seismicity, *J. geophys. Res.,* **117**(B09306), doi:10.1029/2012JB009407.

Moulik, P. & Ekström, G., 2014) An anisotropic shear velocity model of the Earth's mantle using normal modes, body waves, surface waves and long-period waveforms, *Geophys. J. Int.,* **199**(3), 1713–1738.

Nabelek, J. & Braunmiller, J., 2013. Seismicity, structure and dynamics of the Gorda deformation zone, International Federation of Digital Seismograph Networks, Other/Seismic Network, 10.7914/SN/Z5_2013.

Nedimović, M.R., Bohnenstiehl, D.R., Carbotte, S.M., Pablo Canales, J. & Dziak, R.P., 2009. Faulting and hydration of the Juan de Fuca plate system, *Earth planet. Sci. Lett.,* **284**(1-2), 94–102.

Nedimović, M.R., Hyndman, R.D., Ramachandran, K. & Spence, G.D., 2003. Reflection signature of seismic and aseismic slip on the northern Cascadia subduction interface, *Nature,* **424**(6947), 416–420.

Nishimura, C.E. & Forsyth, D.W.D.W., 1988. Rayleigh waves phase velocities in the Pacific with implications for azimuthal anisotropy and lateral heterogeneities, *Geophys. J. Int.,* **94,** 479–501.

Parsons, T. *et al.*, 1998. A new view into the Cascadia subduction zone and volcanic arc: implications for earthquake hazards along the Washington margin, *Geology,* **26**(3), 199–202.

Peterson, J., 1993. Observations and modeling of seismic background noise. U.S. Geol. Surv., Open-File Report 93–322, pp. 95.

Porritt, R.W., Allen, R.M., Boyarko, D.C. & Brudzinski, M.R., 2011. Investigation of Cascadia segmentation with ambient noise tomography, *Earth planet. Sci. Lett.,* **309**(1-2), 67–76.

Rathnayaka, S. & Gao, H., 2017. Crustal-scale seismic structure from trench to forearc in the Cascadia subduction zone, *J. geophys. Res.,* 122, doi:10.1002/2017JB014299.

Ritsema, J., Deuss, A., van Heijst, H.J. & Woodhouse, J.H., 2011. S40RTS: a degree-40 shear-velocity model for the mantle from new Rayleigh wave dispersion, teleseismic traveltime and normal-mode splitting function measurements, *Geophys. J. Int.,* **184**(3), 1223–1236.

Ruan, Y., Forsyth, D.W. & Bell, S.W., 2014. Marine sediment shear velocity structure from the ratio of displacement to pressure of Rayleigh waves at seafloor, *J. geophys. Res.,* **119,** doi:10.1002/2014JB011162.

Ryan, W.B.F. *et al.*, 2009. Global Multi-Resolution Topography synthesis, *Geochem. Geophys. Geosyst.,* **10,** Q03014, doi:10.1029/2008GC002332.

Rychert, C.A., Harmon, N. & Tharimena, S., 2018. Scattered wave imaging of the oceanic plate in Cascadia, *Sci. Adv.,* **4**(2), eaao1908, doi:10.1126/sciadv.aao1908.

Sherrod, D.R. & Smith, J.G., 1990) Quaternary extrusion rates of the cascade range, northwestern United States and southern British Columbia, *J. geophys. Res.,* **95,** 19465–19474.

Shillington, D.J., Van Avendonk, H.J.A., Holbrook, W.S., Kelemen, P.B. & Hornbach, M.J., 2004. Composition and structure of the central Aleutian island arc from arc-parallel wide-angle seismic data, *Geochem. Geophys. Geosyst.,* **5,** Q10006, doi:10.1029/2004GC000715.

Stein, C.A. & Stein, S., 1992. A model for the global variation in oceanic depth and heat flow with lithospheric age, *Nature,* **359,** 123–129.

Tian, Y. & Ritzwoller, M.H., 2015. Directionality of ambient noise on the Juan de Fuca plate: implications for source locations of the primary and secondary microseisms, *Geophys J. Int.,* **201**(1), 429–443.

Tian, Y., Shen, W. & Ritzwoller, M.H., 2013. Crustal and uppermost mantle shear velocity structure adjacent to the Juan de Fuca ridge from ambient seismic noise, *Geochem. Geophys. Geosyst.,* **14**(8), 3221–3233.

Till, C.B., Kent, A.J., Abers, G.A., Janiszewski, H.A., Gaherty, J.B. & Pitcher, B., 2019. The causes of spatiotemporal variations in erupted fluxes and compositions along a volcanic arc, *Nat. Commun.,* in press, doi.org/10.1038/s41467-019-09113-0.

Toomey, D.R. *et al.*, 2014. The Cascadia Initiative: a sea change in seismological studies of subduction zones, *Oceanography,* **27,** 138–150.

Trehu, A.M., Asudeh, I., Brocher, T.M., Luetgert, J.H., Mooney, W.D., Nabelek, J.L. & Nakamura, Y., 1994. Crustal architecture of the Cascadia forearc, *Science,* **266**(5183), 237–243.

Turcotte, D.L. & Schubert, G., 1982. *Geodynamics: Applications of Continuum Physics to Geological Problems,* John Wiley and Sons, Inc.

Van Avendonk, H.J.A., Holbrook, W.S., Lizarralde, D. & Denyer, P., 2011. Structure and serpentinization of the subducting Cocos plate offshore Nicaragua and Costa Rica, *Geochem. Geophys. Geosyst.,* **12**(6), doi:10.1029/2011GC003592.

Wagner, L., Forsyth, D.W., Fouch, M.J. & James, D.E., 2010. Detailed three-dimensional shear wave velocity structure of the northwestern United States from Rayleigh wave tomography, *Earth planet. Sci. Lett.,* **299**(3-4), 273–284.

Wang, P.-L., Engelhart, S.E., Wang, K., Hawkes, A.D., Horton, B.P., Nelson, A.R. & Witter, R.C., 2013. Heterogeneous rupture in the great Cascadia earthquake of 1700 inferred from coastal subsidence estimates, *J. geophys. Res.,* **118**(5), 2460–2473.

Webb, S.C. & Crawford, W.C., 2010. Shallow-water broadband OBS seismology, *Bull. seism. Soc. Am.,* **100**(4), 1770–1778.

Wech, Aaron G., 2010. Interactive Tremor Monitoring, *Seismological Research Letters,* **81**(4), 664–669, doi.org/10.1785/gssrl.81.4.664.

Wei, S.S., Zha, Y., Shen, W., Wiens, D.A., Conder, J.A. & Webb, S.C., 2016. Upper mantle structure of the Tonga-Lau-Fiji region from Rayleigh wave tomography, *Geochem. Geophys. Geosyst.,* **17**(11), 4705–4724.

Wells, R.E., Blakely, R.J., Sugiyama, Y., Scholl, D.W. & Dinterman, P.A., 2003. Basin-centered asperities in great subduction zone earthquakes: a link between slip, subsidence, and subduction erosion? *J. geophys. Res.,* **108**(B10), doi:10.1029/2002JB002072.

Wells, R.E., Blakely, R.J., Wech, A.G., McCrory, P.A. & Michael, A., 2017. Cascadia subduction tremor muted by crustal faults, *Geology,* **45**(6), 515–518.

Wiens, D.A., Conder, J.A. & Faul, U., 2008. The seismic structure and dynamics of the mantle wedge, *Annu. Rev. Earth Planet. Sci.,* **36,** 421–455.

Wilson, D.S., 1993. Confidence intervals for motion and deformation of the Juan de Fuca plate, *J. geophys. Res.,* **98,** 16 053–16 701.

Yao, H., Gouédard, P., Collins, J.A., McGuire, J.J. & van der Hilst, R.D., 2011. Structure of young East Pacific Rise lithosphere from ambient noise correlation analysis of fundamental- and higher-mode Scholte-Rayleigh waves, *C. R. Geosci.,* **343**(8-9), 571–583.